IEEE Open Journal of Vehicular Technology

Received XX Month, XXXX; revised XX Month, XXXX; accepted XX Month, XXXX; Date of publication XX Month, XXXX; date of current version XX Month, XXXX.

Digital Object Identifier 10.1109/XXX

IM-OFDM ISAC Outperforms OFDM ISAC By Combining Multiple Sensing Observations

Hugo Hawkins*, ***Graduate Student Member, IEEE,*** **Chao Xu***, ***Senior Member, IEEE,*** **Lie-Liang Yang***, ***Fellow, IEEE*** **and Lajos Hanzo*** ***Life Fellow, IEEE***

[1]School of Electronics and Computer Science, University of Southampton, Southampton SO17 1BJ, U.K.

Corresponding Author: Lajos Hanzo (e-mail: lh@ecs.soton.ac.uk).

ABSTRACT Index Modulated Orthogonal Frequency-Division Multiplexing (IM-OFDM) based Integrated Sensing and Communication (ISAC) is potentially capable of outperforming Orthogonal Frequency-Division Multiplexing (OFDM) ISAC, since Index Modulation (IM) concentrates increased power on the activated subcarriers. This has been confirmed by authoritative publications for the IM-OFDM communication component. However, no evidence is found in the open literature that IM-OFDM sensing is capable of outperforming OFDM sensing, because the blank subcarriers impair the system's sensing functionality. The existing solutions either insert a radar signal into the deactivated subcarriers, thereby using a radar signal for sensing, or employ compressed sensing, which leads to a lower sensing performance than OFDM ISAC.

Hence, a novel low complexity algorithm is proposed for ensuring that an IM-OFDM ISAC system outperforms its OFDM ISAC counterpart for both communication and sensing. The algorithm collects observations of the received signal to "fill in" the blank subcarriers in the sensing data created by IM-OFDM, whilst taking advantage of the increased subcarrier power attained by activating fewer subcarriers. This occurs over multiple transmit frames, which inevitably delays the target estimation. As OFDM sensing assumes low target velocities, this delay is shown to have a negligible impact on the sensing performance of IM-OFDM.

The simulation results show that IM-OFDM ISAC is indeed capable of outperforming its OFDM ISAC counterpart for both sensing and communication. The impact of block interleaving and of the modulation type on the sensing performance is also discussed.

INDEX TERMS Integrated Sensing and Communication, Index Modulation, Orthogonal Frequency-Division Multiplexing

I. Introduction

The potential to utilise radio signals for sensing was recognised from the earliest use of radios for communication in the late 19th century, with a variety of systems in use by the early 20th century [1]. Both the military and commercial potentials of this combination were also understood, but there is still a dearth of contemporary studies, apart from some patent applications. Some reviews of this period are available in [2], [3]. The first operational navigation aids were direction finders, whereby a directional aerial is used either to transmit a radio signal, or to detect the heading to an omni-directional radio source. Typically, the source would be transmitting data, initially in the form of Morse code, to identify the source and improve angular resolution.

These analogue systems rapidly developed to include bi-directional communication, triangulation, and Doppler shift sensing for providing both range, direction, and communication functions. Combining these with systems such as the Hellschreiber of [2] permitted semi-automation of the sensing function and the inference of crude guidance indicators, along with improved communication. Whilst having a light spectral utilisation was not an issue in the early years, the

L. Hanzo would like to acknowledge the financial support of the Engineering and Physical Sciences Research Council projects EP/W016605/1, EP/X01228X/1 and EP/Y026721/1 as well as of the European Research Council's Advanced Fellow Grant QuantCom (Grant No. 789028)

employment of benign communication signals for sensing reduced jamming efficacy.

Similar systems, capable of utilising commercial Amplitude Modulation (AM) radio transmitters, remained standard equipment on aircraft until displaced by LORAN-C and GPS at the end of the 20th century. Dedicated digital radio direction finders systems are still used for aircraft approach and landing control, and for marine applications [4]. As the arms race prior to World War 2 commenced, research focus expanded to include radar sensing of passive targets, which relied on a sensing-only function initially, but communication components were soon added as counter-countermeasures.

The modern concept of Integrated Sensing and Communication (ISAC) has found its way into the open scientific literature in 1963, with [5] detailing a system sending communication pulses on the radar pulse interval to transmit information from a base station to vehicles for one way communication. The authors base the system on the capabilities of a missile ranging equipment of that era, and also calculate both the pulse code group and word error probabilities of the communication system.

The system has five pulse slots available per information bit transmitted. The first two are interrogation signals, with the second one being a reference signal. A pulse is transmitted on the first of the three data slots when the information bit is 0, with a pulse on the second slot for a bit of 1. A pulse is sent on the last data slot to indicate the start of a word. The throughput of this early ISAC system is therefore low, since the rate of communication is dictated by the radar pulse interval, and only one bit is transmitted per pulse code group.

Over the years, the spectral efficiency requirement of ISAC has increased as the spectrum has become more congested due to the increase in wireless devices. ISAC is also expected to become a fundamental component of the future Internet of Things (IoT), and has matured due to improvements in technology, as a benefit of convergence between the sensing and communication protocols.

The advantages of ISAC include the reduction in weight, size and power consumption of a combined system [6], [7], and minimising spectral congestion [8]. The signal processing techniques of mmWave and massive Multiple Input Multiple Output (MIMO) bear some similarities to those of MIMO radar [9]. The advantages of MIMO for both communication and radar are similar, supporting both spatial diversity [10], [11] and flexible beamforming [12]. Channel information can be estimated by exploiting the sensing signals, while supporting communication [13].

Communication-centric ISAC systems have been the subject of much research. There are some systems that consider single carrier waveforms [14], [15]. ISAC has also been investigated using Orthogonal Frequency-Division Multiplexing (OFDM) [6], [15]–[22], and the more recent Orthogonal Time Frequency Space (OTFS) schemes [23]–[25]. Given the existing commercial implementations of OFDM for communication, there is much interest in its potential use in ISAC. OFDM has been shown to be suitable for ISAC in [15], where a physical system was tested.

However, publications are sparse on the subject of Frequency Domain (FD) Index Modulation (IM) aided ISAC. The authors of [26] use circularly-shifted chirps based on the DFT-spread-OFDM structure in conjunction with IM and Phase Shift Keying (PSK) modulation for ISAC. The chirps are sent along frequencies dictated by the subcarrier indices. The transmitted signal is similar in structure to an Index Modulated Orthogonal Frequency-Division Multiplexing (IM-OFDM) signal, with the signal on the activated subcarriers being chirps with embedded PSK symbols created through FD spectral shaping. No comparisons are made with conventional OFDM ISAC.

Another system that incorporates frequency IM for ISAC is [27]. This system uses carrier agile phased array radar for sensing, whilst communicating using both FD and Antenna Domain (AD) IM. The available frequencies are divided into subcarrier groups, with the frequencies transmitted by each antenna being dictated by the FD and AD indices. The throughput of this system remains much lower than that of the equivalent systems utilising communication waveforms. The companion paper [28] considers the scenario where the system is used exclusively for sensing. The results show that the sensing performance is lower than that of the Frequency-Agile Radar (FAR) concept in all conditions considered.

The system in [29] considers the combination of IM and of the Frequency-Diverse Array (FDA) radar, with the addition of phase modulation applied to the transmitted radar signals. The introduction of IM leads to higher sidelobes in the beampattern used for range estimation, but it is shown to have no significant effect on the beampattern harnessed for angle estimation. The Cramér-Rao Bound (CRB) of the proposed system is also shown to be lower than that of traditional FDA radar systems.

The authors of [30] develop a general Frequency Hopping (FH) MIMO model for ISAC, which can be tuned for harnessing multiple communication strategies. These are conventional data modulation, such as Quadrature Amplitude Modulation (QAM) or PSK, IM, and FH code selection. The transmitted signal is split into separate matrices, each representing a specific communication signaling strategy. The pair of hybrid communication strategies considered are the combination of PSK and FH code selection, as well as the combination of FH code selection and IM. The Bit Error Rate (BER) of the hybrid schemes constitutes a middle ground between the BER of the individual constituent signaling strategies. The sidelobe levels of the hybrid schemes are dominated by the highest sidelobe levels of the component signaling strategies. This leads to a trade-off between the communication throughput and sensing performance.

IM can also be implemented in conjunction with FAR. The authors of [7] undertake a numerical evaluation of

OFDM and IM-FAR, under Rayleigh fading but in the absence of interference, whilst ensuring that both systems have the same throughput. Their results show that both systems have a similar sensing Mean Square Error (MSE) performance, with OFDM having a significantly superior BER performance over IM-FAR. The authors postulate that the IM-FAR sensing performance would be higher than that of OFDM, when there are multiple devices, since IM-FAR has a low mutual interference [28].

Combining IM and OFDM has the potential of increasing the implementation and energy efficiencies, the robustness to interference and noise, and is therefore capable of improving the communication BER performance [13]. IM-OFDM partitions the OFDM subcarriers into groups, with a subset of the subcarriers in each group being activated. The activated subcarriers transmit signals, with the indices of the activated subcarriers also conveying information.

The IM-OFDM structure leads to a condition in which IM-OFDM communication can always outperform OFDM: for an M-QAM/PSK OFDM system where each transmitted signal has an average power of 1, the IM-OFDM system should have M subcarriers with $M-1$ activated subcarriers in each group. This allows the IM-OFDM system to use M-QAM/PSK, which maintains the throughput of the OFDM system, with each transmitted signal having an average power of $\sqrt{\frac{M}{M-1}}$.

The primary issue caused by IM-OFDM for ISAC is the lack of a signal transmitted on certain subcarriers, since this creates "holes" in the reflected signal from a sensing target. Hence different methods have been proposed for mitigating this issue.

A method is to use compressed sensing as in [31], where the transmitted signal is a typical IM-OFDM signal. A compressed sensing problem is formulated based on the received signal, in an attempt to interpolate the missing information. This method leads to a slightly poorer sensing performance than OFDM sensing, but retains the improved communication performance of IM-OFDM over OFDM.

A second method is to use frequency-agile radar in conjunction with IM-OFDM communication, as proposed in [13]. In this system, radar signals are sent over some of the deactivated communication subcarriers, avoiding the use of IM-OFDM for sensing. Şahin et al. [13] consider bistatic sensing, allowing the communication receiver to use the radar signals for channel estimation. These techniques are shown to allow for a similar communication performance to that of conventional OFDM pilot signals. The method of [13] does not fully integrate sensing and communication, since two separate types of signal are transmitted.

The aim of this work is to develop an IM-OFDM ISAC system that outperforms an OFDM ISAC system for both communication and sensing.

The existing published work either inserts a radar signal into the deactivated subcarriers, thereby using a radar signal for sensing, or employs compressed sensing, which leads to a lower sensing performance than OFDM ISAC.

Hence, a novel low complexity algorithm is proposed that collects observations of the received signal to "fill in" the "holes" in the sensing data created by IM-OFDM, whilst taking advantage of the increased signal power gleaned from activating fewer subcarriers. This occurs over multiple transmit frames, which delays the target estimation. As OFDM sensing assumes low target velocities, this delay is shown to have a negligible impact on the sensing performance of IM-OFDM.

The simulation results will demonstrate that an IM-OFDM ISAC scheme is capable of outperforming its OFDM ISAC counterpart for both sensing and communication. The impact of block interleaving and of the modulation type on the sensing performance are also discussed. Since IM-OFDM sensing removes the data from the received signal, block interleaving has no significant impact on the sensing performance, which is validated through the simulation results.

Two modulation types are considered, PSK and QAM. As PSK maintains a constant amplitude, the transmitted data has no significant effect on its sensing performance. This is true, regardless of the modulation order. By contrast, varying the QAM modulation order has a substantial impact on the system's sensing performance, caused by the increased number of possible amplitude levels, as the QAM modulation order is increased. Due to this, sensing using PSK outperforms sensing with QAM at modulation orders higher than 4, as Binary Phase Shift Keying (BPSK) and Quadrature Phase Shift Keying (QPSK) have the same constellations as 2-QAM and 4-QAM, respectively.

A. Contributions

This work's contributions are boldly contrasted to the literature in Table 1, and are detailed below:

- A novel low complexity algorithm is conceived to "fill in" the "holes" in the sensing data created by IM-OFDM, whilst taking advantage of the increased subcarrier power gleaned from activating fewer subcarriers. This allows IM-OFDM sensing to outperform OFDM, with a slight increase in delay. As OFDM sensing assumes a low-Doppler environment, the impact of this sensing delay increase is negligible.
- An analysis of the impact of block interleaving and QAM/PSK on sensing performance.

The notations used are shown in Table 2.

II. System Model

This section presents the system model and its underlying assumptions. The system considers point-to-point transmission between two communication devices, and sensing of multiple targets.

It is assumed that there is no external interference during transmission. For communication, integer delay indices are

TABLE 1: Contrasting on contributions to the literature

Topics \ Papers	[31]	[26]	[27]	[13]	[15]	[16]	[23]	This work
Channel modeling								
Doubly selective channel model				✓		✓	✓	✓
System								
IM-OFDM	✓			✓				✓
Frequency IM	✓	✓	✓	✓				✓
Reduced PAPR compared to OFDM	✓	✓	✓	✓			✓	✓
Improved data efficiency compared to OFDM	✓	✓	✓				✓	✓
Combining multiple observations for sensing								✓
Results								
BER and RMSE improvements to OFDM sensing whilst maintaining throughput								✓
Effect of block interleaver on sensing RMSE								✓
Effect of PSK and QAM modulation on RMSE								✓

TABLE 2: Notations

Definition	Example	Description
Scalar value	a/A	Italics
Vector	$\boldsymbol{a}$	Bold lower case
Matrix	$\boldsymbol{A}$	Bold upper case
Vector or matrix transpose	$(\cdot)^T$	
Complex conjugate operation	$(\cdot)^*$	
Complex conjugate transpose	$(\cdot)^H$	
Inverse of a matrix	$(\cdot)^{-1}$	

assumed, as discussed in Section 2, along with perfect channel estimation. For sensing, it is assumed that there is a single Line of Sight (LoS) path between the transmitter and each target, with the number and directions of the targets being known. The Cyclic Prefix (CP) is assumed to be sufficiently long to avoid Inter-Symbol Interference (ISI), which is perfectly removed from the received signal at the receiver. The channel's Doppler shifts are less than a tenth of the subcarrier spacing, to correlate with other studies, but this is not a limitation of this system, as a time and frequency selective channel is modeled.

A. Transmitted Signal

To implement IM-OFDM, the M subcarriers of the system are partitioned into G subcarrier groups. Hence, each group contains $\frac{M}{G} = M_G$ subcarriers. For IM, M_A subcarriers are activated in each group at any given time, with $M_A < M_G$. Since the total available power is constant, as and when fewer subcarriers are activated, additional power is allocated to the activated subcarriers. Therefore, the ratio of power assigned to each activated subcarrier of IM-OFDM compared to an equivalent OFDM system having the same throughput is $\frac{M_G}{M_A}$.

The number of bits determining the activated subcarrier indices of a group is $\beta_G = \lfloor log_2 \mathcal{C}_{M_G}^{M_A} \rfloor$, where $\lfloor \cdot \rfloor$ is the floor function, and $\mathcal{C}_{M_G}^{M_A}$ is the total number of permutations of M_A in M_G indices. Correspondingly, the number of possible subcarrier combinations used for IM within a group is $C_N = 2^{\beta_G}$. The C_N subcarrier combinations are collected to form a set, expressed as $\mathfrak{C} \in \mathbb{Z}^{C_N \times M_A}$. On each of the activated subcarrier, a Γ-PSK or Γ-QAM symbol is transmitted, with each symbol conveying $\beta_\Gamma = log_2(\Gamma)$ bits. Therefore, the total number of bits β transmitted per IM-OFDM symbol is $\beta = G\left(\beta_G + M_A \beta_\Gamma\right)$.

In this IM-OFDM system, block interleaving is employed for distributing the activated subcarriers from each group across the entire available bandwidth, dispersing the subcarriers across all groups. This minimises the probability that an entire group of subcarriers will experience similar fading, and hence increases the communication reliability. Specifically, the block interleaving process is described as:

$$\bar{\boldsymbol{x}}_{bi,\,n}[\bar{m}_G G + g] = \bar{\boldsymbol{x}}_n[gG + \bar{m}_G] \ , \tag{1}$$

where $\bar{\boldsymbol{x}}_n \in \mathbb{C}^{M \times 1}$ is the vector of modulated data for the n^{th} IM-OFDM FD symbol, $\bar{\boldsymbol{x}}_{bi,\,n} \in \mathbb{C}^{M \times 1}$ is the vector of modulated data after block interleaving, $n = 0, ..., N-1$ is the IM-OFDM symbol index, with N being the number of IM-OFDM symbols transmitted in a frame, $\bar{m}_G = 0, ..., M_G - 1$ is the subcarrier index within a group, and $g = 0, ..., G-1$ is the subcarrier group index.

After block interleaving, the Inverse Discrete Fourier Transform (IDFT) is applied to $\bar{\boldsymbol{x}}_{bi,\,n}$ to determine the Time Domain (TD) signals for transmission, which is expressed as:

$$\boldsymbol{x}_n = \mathcal{F}_M^{-1}\left(\bar{\boldsymbol{x}}_{bi,\,n}\right) \ , \tag{2}$$

where $\boldsymbol{x}_n \in \mathbb{C}^{M \times 1}$ is the transmitted baseband TD signal, and $\mathcal{F}_M^{-1}$ is the M-point IDFT.

Again, it is assumed that the CP is long enough to guarantee that there is no ISI between adjacent OFDM symbols. It is also assumed that it is perfectly removed from the received signal, thereby having no detrimental effect

on the system performance. Consequently, the CP is not considered any further.

B. Channel Models and Received Signal

The transmitted signal is passed through a time and frequency selective fading channel, as modelled in [32]. The Delay-Doppler Domain (DD) representation of the fading channel is:

$$\tilde{h}(\tau, \nu) = \sum_{l=0}^{L-1} P_l \tilde{h}_l \delta(\tau - \tau_l)\delta(\nu - \nu_l) \ , \tag{3}$$

where τ is the delay, ν is the Doppler shift, l is the propagation path index, L is the total number of propagation paths, τ_l is the delay associated with the l^{th} path, ν_l is the Doppler shift associated with the l^{th} path, P_l is the path loss associated with the l^{th} path, $\tilde{h}_l$ is the fading gain associated with the l^{th} path, and $\delta(\cdot)$ is the Dirac delta function.

When sampled in the DD, the channel can be represented by time-invariant fading gain $\tilde{h}_l$, delay index τ_i, and Doppler index ν_i. The delay and Doppler indices are defined as:

$$\tau_i = (\Delta f M)\tau \tag{4}$$

$$\nu_i = \frac{N}{\Delta f}\nu \ , \tag{5}$$

where Δf is the subcarrier spacing.

The TD representation of the fading channel is therefore:

$$h_{m,\,n,\,l} = P_l \tilde{h}_l e^{j2\pi\nu_{i,\,l}\frac{nM+m-\tau_{i,\,l}}{MN}} \ , \tag{6}$$

where $j = \sqrt{-1}$, m is the sample index, while $\tau_{i,\,l}$ and $\nu_{i,\,l}$ are the delay and Doppler indices associated with the l^{th} propagation path.

The received TD signal $\boldsymbol{y}_n \in \mathbb{C}^{M\times 1}$ is expressed as:

$$\boldsymbol{y}_n[m] = \sum_{l=0}^{L-1} h_{m,\,n,\,l}\ \boldsymbol{x}_n[m - \tau_{i,\,l}] + \boldsymbol{z}_n[m] \ , \tag{7}$$

where $\boldsymbol{z}_n$ is the complex Additive White Gaussian Noise (AWGN), with mean $\mu_z = 0$ and variance σ_z^2, expressed as $\mathcal{N}(\mu_z, \sigma_z^2)$, and $\boldsymbol{x}_n[m - \tau_{i,\,l}]$ is the delayed transmitted baseband TD signal propagating through the l^{th} path, with $\boldsymbol{x}_n \in \mathbb{C}^{M\times 1}$.

When the delay indices of the propagation paths are assumed to be integers, the fading channel and the received signal can be modelled as in (7). When this assumption is discarded, the values of m, at which $m-\tau_{i,\,l}$ is an integer, no longer coincide with the integer matrix indices. As matrices do not have fractional indices, the channel has to be modelled differently. A portion of the fading channel is modelled in the FD, then converted to the TD as follows:

$$\boldsymbol{x}_n[m - \tau_{i,\,l}] = \frac{1}{\sqrt{M}} \sum_{\bar{m}=0}^{M-1} \bar{\boldsymbol{x}}_{bi,\,n}[\bar{m}] e^{j2\pi\frac{(m-\tau_{i,\,l})\bar{m}}{M}} \ , \tag{8}$$

where $\bar{m}$ is the subcarrier index.

The received TD signal becomes:

$$\boldsymbol{y}_n[m] = \frac{1}{\sqrt{M}} \sum_{l=0}^{L-1} h_{m,\,n,\,l} \sum_{\bar{m}=0}^{M-1} \bar{\boldsymbol{x}}_{bi,\,n}[\bar{m}] e^{j2\pi\frac{(m-\tau_{i,\,l})\bar{m}}{M}} + \boldsymbol{z}_n[m] \ . \tag{9}$$

Equation (9) is more computationally demanding than equation (7), because for each IM-OFDM symbol, ML IDFTs are taken, as opposed to having a single IDFT for integer indices.

1) Sensing

For simplicity, having a single propagation path spanning from the source to the sensing target is assumed, since the power of the scattered Non-Line of Sight (NLoS) paths is considered negligible compared to the power of the LoS paths. The fading gain $\tilde{h}_{l,\,sen}$ and the path loss $P_{l,\,sen}$ for the l_{sen}^{th} target are:

$$\tilde{h}_{l,\,sen} = 1 \tag{10}$$

$$P_{l,\,sen} = \sqrt{\frac{c_0^2 \gamma_l}{(4\pi)^3 f_c^2 R_{l,\,sen}^4}} \ , \tag{11}$$

where $(\cdot)_{sen}$ denotes a sensing variable, c_0 is the speed of light, f_c is the carrier frequency, γ_l is the radar cross-section of target l_{sen}, and $R_{l,\,sen}$ is the distance between the sensing target l_{sen} and the transmitter. The total number of sensing targets is L_{sen}.

Given $R_{l,\,sen}$ and the velocity $V_{l,\,sen}$ of the l_{sen}^{th} target, the delay $\tau_{l,\,sen}$ and Doppler shift $\nu_{l,\,sen}$ of the l_{sen}^{th} target are:

$$\tau_{l,\,sen} = \frac{2}{c_0} R_{l,\,sen} \tag{12}$$

$$\nu_{l,\,sen} = \frac{2 f_c}{c_0} V_{l,\,sen} \ . \tag{13}$$

The associated delay and Doppler indices are determined following (4) and (5).

2) Communication

The communication path loss is formulated as:

$$P_{l,\,com} = \sqrt{\frac{c_0^2}{(4\pi)^2 f_c^2 R_{com}^2}} \ , \tag{14}$$

where $(\cdot)_{com}$ denotes a communication variable, while R_{com} is the distance from the transmitter to the receiver.

The communication channel is assumed to have L_{com} propagation paths, where the first path of $l_{com} = 0$ is the LoS path, and the subsequent $L_{com} - 1$ paths are NLoS paths. Hence, following [32], the fading gains of the communication paths can be expressed as:

$$\tilde{h}_{l,com} = \begin{cases} \sqrt{\frac{K}{K+1}}, & \text{if } l_{com} = 0 \\ \sqrt{\frac{1}{(K+1)(L_{com}-1)}}\zeta_{l,com}, & \text{if } 0 < l_{com} \leq L-1, \end{cases} \tag{15}$$

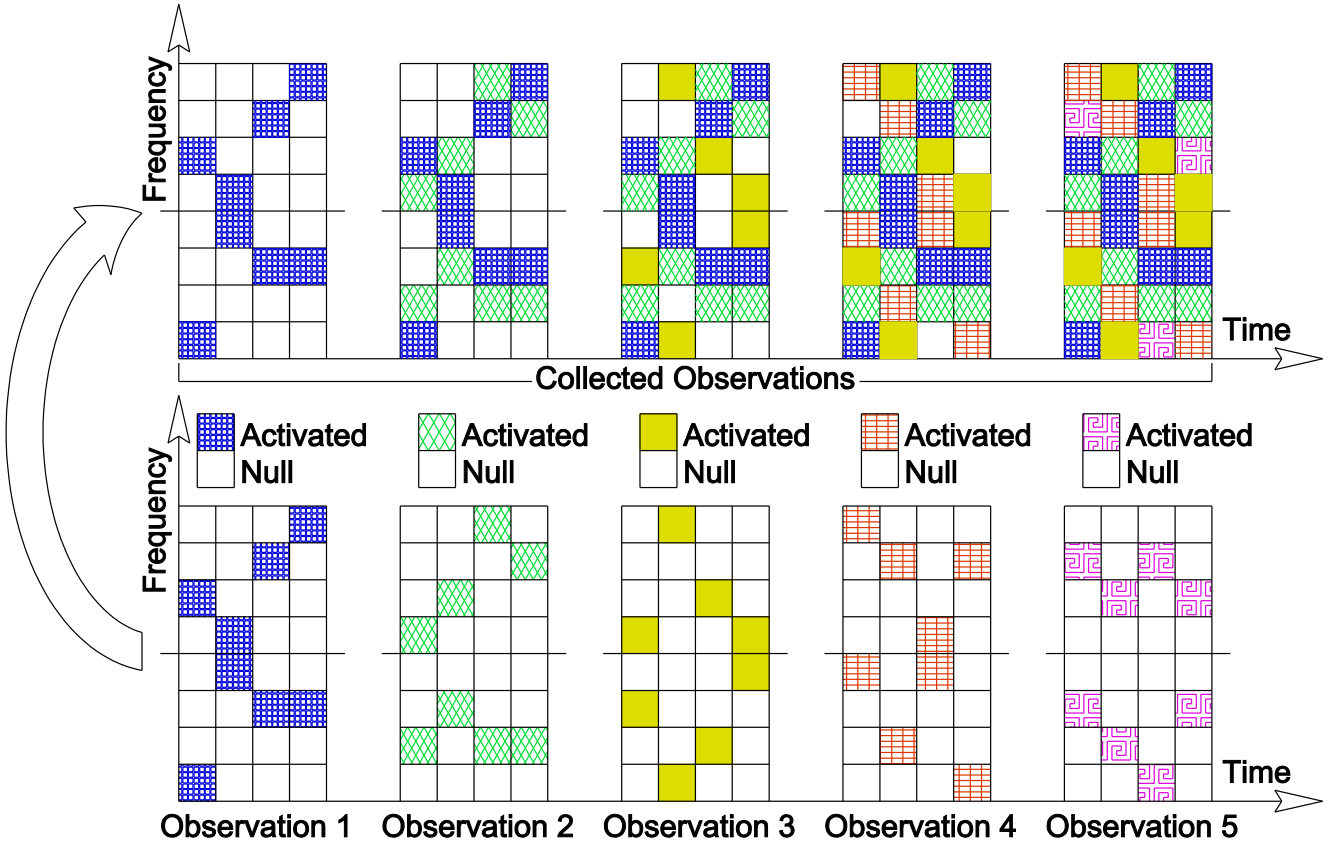

FIGURE 1: Example to illustrate the observation collection for $M = 8$, $N = 4$, $M_G = 4$, $M_A = 1$, and $N_{CL} = 5$

where K is the Rician K factor, and $\zeta_{l,\,com}$ is a complex Gaussian random variable having a mean of $\mu_{com} = 0$ and a variance of $\sigma^2_{com} = 1$, expressed as $\mathcal{N}(0,\, \sigma^2_{com})$.

As the signal transmitted along the LoS path is the first to arrive at the receiver, its delay can be set to 0. The delays associated with the propagation paths for communication are denoted as:

$$\tau_{l,\,com} = \begin{cases} 0\ , & \text{if } l = 0 \\ \tau_{max,\,com}\eta_\tau\ , & \text{if } 0 < l_{com} \leq L-1\ , \end{cases} \tag{16}$$

where η_τ is a random variable following a uniform distribution between 0 and 1, and $\tau_{max,\,com}$ is the maximum propagation path delay, defined as:

$$\tau_{max,\,com} = \frac{L_{com}}{\Delta f M}\ . \tag{17}$$

The Doppler shift of each communication path is:

$$\nu_{l,com} = \begin{cases} \nu_{com}, & \text{if } l = 0 \\ \nu_{max,com}(\eta_\nu - 0.5), & \text{if } 0 < l_{com} \leq L-1, \end{cases} \tag{18}$$

where ν_{com} is the Doppler shift of the communication receiver, $\nu_{max,\,com}$ is the maximum Doppler shift, and η_ν is a random variable following a uniform distribution between 0 and 1. The Doppler shift and maximum Doppler shift of the communication receiver are:

$$\nu_{com} = \frac{f_c}{c_0} V_{com} \tag{19}$$

$$\nu_{max,\,com} = \frac{\Delta f}{N} \lceil \frac{N}{\Delta f} \nu_{com} \rceil\ , \tag{20}$$

where V_{com} is the communication target velocity, and $\lceil \cdot \rceil$ is the ceiling function.

III. Object Sensing and Signal Detection

This section describes the target detection and parameter estimation for sensing, and the signal detection considered in communication. For both sensing and communication, the received TD signal $\boldsymbol{y_n}$ is first converted to the FD before processing:

$$\bar{\boldsymbol{y}}_n = \mathcal{F}_M\left(\boldsymbol{y}_n\right)\ , \tag{21}$$

where $\mathcal{F}_M$ is the M-point Discrete Fourier Transform (DFT).

A. Object Sensing

Following [16], the FD received signal can be expressed as:

$$\bar{\boldsymbol{y}}_{n,\,sen}[\bar{m}] = \bar{\boldsymbol{x}}_{bi,\,n}[\bar{m}] \sum_{l=0}^{L-1} P_{l,\,sen}\tilde{h}_{l,\,sen} \times \left(\boldsymbol{a}(\tau_{i,\,l,\,sen})\boldsymbol{a}(\nu_{i,\,l,\,sen})^T\right)_{\bar{m},\,n} + \bar{\boldsymbol{z}}_n[\bar{m}] \;, \quad (22)$$

where $\bar{m} = 0, ..., M-1$, $n = 0, ..., N-1$, $\bar{\boldsymbol{z}}_n$ is the FD AWGN, while $\boldsymbol{a}(\tau_{i,\,l,\,sen}) \in \mathbb{C}^{M\times 1}$ and $\boldsymbol{a}(\nu_{i,\,l,\,sen}) \in \mathbb{C}^{N\times 1}$ are the delay and Doppler shift index steering vectors, respectively, defined as:

$$\boldsymbol{a}(\tau_{i,\,l,\,sen})[\bar{m}] = e^{-j2\pi\frac{\bar{m}\tau_{i,\,l,\,sen}}{M}} \quad (23)$$

$$\boldsymbol{a}(\nu_{i,\,l,\,sen})[n] = e^{j2\pi\frac{n\nu_{i,\,l,\,sen}}{N}} \;. \quad (24)$$

The delay and Doppler shift information of the target can therefore be determined from the received signal, as long as there are signals transmitted on a sufficient number of subcarriers. However, IM-OFDM does not transmit signals on all subcarriers within each time-slot, as seen in the bottom row of Figure 1, which leads to a lack of target information in the reflected signal. To mitigate this problem, an observation collection matrix is constructed by collecting observations over N_{CL} transmit frames so that most of the missing subcarriers can be filled by signals. This is illustrated in Figure 1, for an IM-OFDM system having 2 groups of 4 subcarriers, where 1 subcarrier is activated in each group. Furthermore, each frame contains 4 IM-OFDM symbols, and five frames are collected to form the time-frequency observation matrix for sensing.

To elaborate, in Figure 1, the top row depicts the matrix of collected observations $\bar{\boldsymbol{Y}}_{CL} \in \mathbb{C}^{M\times N}$ filled with the newly received observations, once they become available. The bottom row shows the individual observations of the 5 frames, each representing a time-frequency matrix $\bar{\boldsymbol{Y}}_{n_{CL}} = \left(\bar{\boldsymbol{y}}_{0,\,n_{CL},\,sen},\, \bar{\boldsymbol{y}}_{1,\,n_{CL},\,sen},\, ...,\, \bar{\boldsymbol{y}}_{N-1,\,n_{CL},\,sen}\right)$ of a specific frame. Prior to an observation matrix being collected, the modulated communication data symbols are removed from the received reflected signals by the transmitter, producing the matrix $\bar{\boldsymbol{U}}_{n_{CL}} \in \mathbb{C}^{M\times N}$, by relying on the operation expressed as:

$$\bar{\boldsymbol{U}}_{n_{CL}} = \bar{\boldsymbol{Y}}_{n_{CL}} \oslash \bar{\boldsymbol{X}}_{bi,\,n_{CL}} \;, \quad (25)$$

where $\bar{\boldsymbol{X}}_{bi,\,n_{CL}} = (\bar{\boldsymbol{x}}_{bi,\,0,\,n_{CL}},\, \bar{\boldsymbol{x}}_{bi,\,1,\,n_{CL}},\, ...,\, \bar{\boldsymbol{x}}_{bi,\,N-1,\,n_{CL}})$ are the data symbols for the n_{CL}^{th} frame, and $\oslash$ is the Hadamard division or element-wise division. When an element of $\bar{\boldsymbol{X}}_{bi,\,n_{CL}}$ is 0, the corresponding element of $\bar{\boldsymbol{U}}_{n_{CL}}$ is set to 0.

Then, as a new observation matrix is collected, the matrix of collected observations $\bar{\boldsymbol{Y}}_{CL}$ in the top row of Figure 1 is updated with the new observation. If there is an overlap between an existing and a new element of an observation, the oldest element is retained. Once all observations over N_{CL} frames have been collected, the delay and Doppler indices of the targets are estimated from the matrix of collected observations $\bar{\boldsymbol{Y}}_{CL}$. This is achieved, following [16], by applying the N-point DFT to the rows and the M-point IDFT to the columns of the matrix of collected observations $\bar{\boldsymbol{Y}}_{CL}$, converting the time-frequency $\bar{\boldsymbol{Y}}_{CL}$ into the DD $\tilde{\boldsymbol{Y}}_{CL} \in \mathbb{C}^{M\times N}$, expressed in (26), where $\tilde{\boldsymbol{Z}} \in \mathbb{C}^{M\times N}$ is the DD matrix of the time-frequency AWGN $\bar{\boldsymbol{Z}}_{n_{CL}} \oslash \bar{\boldsymbol{X}}_{bi,\,n_{CL}}$ collected.

The modulus peaks of $\tilde{\boldsymbol{Y}}_{CL}$ are at $\sum_{l=0}^{L-1}[\tau_i = \lfloor\tau_{i,\,l,\,sen}\rceil,\, \nu_i = \lfloor\nu_{i,\,l,\,sen}\rceil]$ in the absence of noise, where $\lfloor\cdot\rceil$ is the rounding function. Hence, the sensing algorithm estimates the sensing delay indices $\hat{\tau}_{i,\,l,\,sen}$ and Doppler shift indices $\hat{\nu}_{i,\,l,\,sen}$ of the targets by selecting the L modulus peaks of $\tilde{\boldsymbol{Y}}_{CL}$. The estimated target range $\hat{R}_{l,\,sen}$ and velocity $\hat{V}_{l,\,sen}$ are then formulated as:

$$\hat{R}_{l,\,sen} = \hat{\tau}_{i,\,l,\,sen}\frac{c_0}{2\Delta f M} \quad (27)$$

$$\hat{V}_{l,\,sen} = \begin{cases} \hat{\nu}_{i,\,l,\,sen}\frac{\Delta f c_0}{2Nf_c} \;, & \text{if } \hat{\nu}_{i,\,l,\,sen} \le \frac{N}{2} \\ (\hat{\nu}_{i,\,l,\,sen} - N)\frac{\Delta f c_0}{2Nf_c} \;, & \text{if } \hat{\nu}_{i,\,l,\,sen} > \frac{N}{2} \;. \end{cases} \quad (28)$$

Note that for the estimated Doppler index, a value higher than $\frac{N}{2}$ indicates a target having a negative velocity.

When the delay and Doppler indices for a target do not coincide with an integer multiple of the estimation resolution, a finer estimation of the target delay and Doppler indices is beneficial. Following [23], [33], the N-point DFT and M-point IDFT matrices applied to $\tilde{\boldsymbol{Y}}_{CL}$ are substituted by a $(N \times NN_{ML})$ DFT matrix $\boldsymbol{F}_{N\times NN_{ML}}$ and a $(MN_{ML} \times M)$ IDFT matrix $\boldsymbol{F}^{-i}_{MN_{ML}\times M}$, respectively, defined as:

$$\boldsymbol{F}_{N\times NN_{ML}}[n,\, n_{ML}] = \frac{1}{\sqrt{N}} e^{-j2\pi n\frac{n_{ml}}{NN_{ML}}} \quad (29)$$

$$\boldsymbol{F}^{-i}_{MN_{ML}\times M}[\bar{m}_{ML},\, \bar{m}] = \frac{1}{\sqrt{M}} e^{j2\pi\bar{m}\frac{\bar{m}_{ml}}{MN_{ML}}} \;, \quad (30)$$

where $n_{ML} = (0,\, 1,\, ...,\, NN_{ML} - 1)$, $\bar{m}_{ML} = (0,\, 1,\, ...,\, MN_{ML} - 1)$, and N_{ML} is a resolution refinement factor.

The resultant sensing imaging matrix is $\tilde{\boldsymbol{Y}}_{ML} \in \mathbb{C}^{MN_{ML}\times NN_{ML}}$. It is important to note that the range of delay and Doppler shift that can be estimated from $\tilde{\boldsymbol{Y}}_{ML}$ is the same as that from $\tilde{\boldsymbol{Y}}_{CL}$, since the estimation range of delay and Doppler shift is defined by the system parameters, not by the sensing algorithm. As $\tilde{\boldsymbol{Y}}_{ML}$ has more elements than $\tilde{\boldsymbol{Y}}_{CL}$, the delay and Doppler estimation resolution is increased by a factor of N_{ML}.

$$\tilde{\boldsymbol{Y}}_{CL}[\tau_i,\, \nu_i] = \frac{1}{\sqrt{MN}} \sum_{l=0}^{L-1} P_{l,\,sen}\tilde{h}_{l,\,sen} \left(\sum_{\bar{m}=0}^{M-1} e^{j2\pi\frac{\bar{m}(\tau_i - \tau_{i,\,l,\,sen})}{M}}\right)\left(\sum_{n=0}^{N-1} e^{j2\pi\frac{n(\nu_{i,\,l,\,sen} - \nu_i)}{N}}\right) + \tilde{\boldsymbol{Z}}[\tau_i,\, \nu_i] \;, \quad (26)$$

The target range and velocity are then estimated similarly, with M and N in (27) and (28) replaced by MN_{ML} and NN_{ML}, respectively, yielding:

$$\hat{R}_{l,\,sen} = \hat{\tau}_{i,\,l,\,sen}\frac{c_0}{2\Delta f M N_{ML}} \tag{31}$$

$$\hat{V}_{l,sen} = \begin{cases} \hat{\nu}_{i,l,sen}\frac{\Delta f c_0}{2NN_{ML}f_c}, & \text{if} \hat{\nu}_{i,l,sen} \leq \frac{NN_{ML}}{2} \\ (\hat{\nu}_{i,l,sen} - NN_{ML})\frac{\Delta f c_0}{2NN_{ML}f_c}, & \text{if} \hat{\nu}_{i,l,sen} > \frac{NN_{ML}}{2}. \end{cases} \tag{32}$$

B. Signal Detection in Communication

Again, it is assumed that there is perfect channel estimation at the receiver. A pair of demodulation schemes are considered, namely single-tap and Minimum Mean Square Error (MMSE) demodulation. Both schemes operate in the FD. Hence, the TD channel $\boldsymbol{H}_{n,\,com} \in \mathbb{C}^{M\times M}$ is converted to the FD as follows:

$$\bar{\boldsymbol{H}}_{n,\,com} = \mathcal{F}_M\left(\boldsymbol{H}_{n,\,com}\right) \ . \tag{33}$$

The received signal in the FD $\bar{\boldsymbol{y}}_n$ can then be expressed as:

$$\bar{\boldsymbol{y}}_{n,\,com} = \bar{\boldsymbol{H}}_{n,\,com}\bar{\boldsymbol{x}}_{bi,\,com} \ , \tag{34}$$

where $\bar{\boldsymbol{x}}_{bi,\,com}$ is defined in (1).

In the context of single-tap demodulation, the communication information is detected for each subcarrier group separately. The system firstly assumes that all of the subcarriers within a group are activated, then it demodulates and remodulates the information on each subcarrier, in an attempt to recreate the transmitted signal on the subcarrier, formulated as:

$$\hat{\boldsymbol{x}}_{g,\,n}[\bar{m}_G] = \mathbb{M}\left[\mathbb{M}^{-1}\left(\boldsymbol{\varphi}_g[\bar{m}_G]\right)\right] \ , \tag{35}$$

where $\hat{\boldsymbol{x}}_{g,\,n} \in \mathbb{C}^{M_G\times 1}$ is the vector of estimated communication symbols transmitted on the subcarriers within the g^{th} subcarrier group, $\mathbb{M}(\cdot)$ is the modulation function, $\mathbb{M}^{-1}(\cdot)$ is the demodulation function, and $\boldsymbol{\varphi}_g \in \mathbb{C}^{M_G\times 1}$ is defined as:

$$\boldsymbol{\varphi}_g[\bar{m}_G]] = \bar{\boldsymbol{y}}_{n,\,com}[gM_G + \bar{m}_G]\frac{(\bar{h}_{\bar{m}_G,\,g,\,n})^*}{||\bar{h}_{\bar{m}_G,\,g,\,n}||^2} \ , \tag{36}$$

where $\bar{h}_{\bar{m}_G,\,g,\,n} = \bar{\boldsymbol{H}}_{n,\,com}[gM_G + \bar{m}_G,\, gM_G + \bar{m}_G]$, and $(\cdot)^*$ is the complex conjugate.

The differences between the received signal and the estimated transmitted signal for all possible C_N subcarrier index combinations are calculated, with the combination yielding the smallest error being chosen according to:

$$\hat{C} = \arg\min_{\forall c}\sum_{\bar{m}_A=0}^{M_A-1}\left(||\boldsymbol{\varphi}_g[\mathfrak{C}[c,\,\bar{m}_A]] - \hat{\boldsymbol{x}}_{g,\,n}[\mathfrak{C}[c,\,\bar{m}_A]]||^2 - ||\boldsymbol{\varphi}_g[\mathfrak{C}[c,\,\bar{m}_A]]||^2\right)\boldsymbol{\kappa}_g[\mathfrak{C}[c,\,\bar{m}_A]] \ , \tag{37}$$

where $c = 0,\, 1,\, ...,\, C_N - 1$ is the subcarrier combination index in a combination, $\hat{C}$ is the estimated activated subcarrier combination, $\bar{m}_A$ is the activated subcarrier index, and $\boldsymbol{\kappa}_g \in \mathbb{C}^{M_G\times 1}$ is defined as:

$$\boldsymbol{\kappa}_g[\bar{m}_G] = ||\bar{h}_{\bar{m}_G,\,g,\,n}||^2 \ . \tag{38}$$

Once the activated subcarrier index combination having the smallest error is estimated, the transmitted bits are determined based on the estimated activated subcarrier combination and the associated modulated symbols.

The MMSE demodulation is similar to single-tap demodulation, but with the channel matrix $\bar{\boldsymbol{H}}_{n,\,com}$ replaced by $\bar{\boldsymbol{H}}_{mmse,\,n}$, and $\bar{\boldsymbol{y}}_{n,\,com}$ replaced by $\bar{\boldsymbol{y}}_{mmse,\,n}$, which are defined as:

$$\bar{\boldsymbol{H}}_{mmse,\,n} = \bar{\boldsymbol{G}}_n\bar{\boldsymbol{H}}_{n,\,com} \tag{39}$$

$$\bar{\boldsymbol{y}}_{mmse,\,n} = \bar{\boldsymbol{G}}_n\bar{\boldsymbol{y}}_{n,\,com} \ , \tag{40}$$

where $\bar{\boldsymbol{G}}_n \in \mathbb{C}^{M\times M}$ is given by:

$$\bar{\boldsymbol{G}}_n = \left(\bar{\boldsymbol{H}}^H_{n,\,com}\bar{\boldsymbol{H}}_{n,\,com} + N_0\boldsymbol{I}_{M\times M}\right)^{-1}\bar{\boldsymbol{H}}^H_{n,\,com} \ , \tag{41}$$

with N_0 being the AWGN power, and $\boldsymbol{I}_{M\times M}$ the M by M identity matrix.

Note that, for OFDM demodulation, $G = M$ and $M_G = M_A = 1$, since all subcarriers are activated.

IV. System Analysis

A. Cramér-Rao Bound

According to [23], the average unbiased estimator CRB for the associated range and velocity estimation are defined as:

$$\hat{\sigma}^2_{l,\,R} \geq \frac{6N_0}{P^2_{l,\,sen}P_{avg}P_{im}(2\pi)^2MN(M^2-1)}\left(\frac{c_0}{2\Delta f}\right)^2 \tag{42}$$

$$\hat{\sigma}^2_{l,\,V} \geq \frac{6N_0}{P^2_{l,\,sen}P_{avg}P_{im}(2\pi)^2MN(N^2-1)}\left(\frac{c_0\Delta f}{2f_c}\right)^2 \ , \tag{43}$$

where $\hat{\sigma}^2_{l,\,R}$ and $\hat{\sigma}^2_{l,\,V}$ are the variance of the target range and velocity estimation errors, respectively, P_{avg} is the average transmit power of the modulated communication symbols before the power allocation due to IM, and P_{im} is the additional power allocated to each activated subcarrier due to IM.

The CRB assumes the best case for IM-OFDM, where there is a complete set of information of the reflected signal. As the Root Mean Square Error (RMSE) is the metric used for sensing, the standard deviation is utilised:

$$\hat{\sigma}_{l,\,R} \geq \sqrt{\frac{6N_0}{P^2_{l,\,sen}P_{avg}P_{im}(2\pi)^2MN(M^2-1)}}\frac{c_0}{2\Delta f} \tag{44}$$

$$\hat{\sigma}_{l,\,V} \geq \sqrt{\frac{6N_0}{P^2_{l,\,sen}P_{avg}P_{im}(2\pi)^2MN(N^2-1)}}\frac{c_0\Delta f}{2f_c} \ , \tag{45}$$

where $\hat{\sigma}_{l,\,R}$ and $\hat{\sigma}_{l,\,V}$ are the standard deviations of the target range and velocity estimation errors, respectively.

It is important to note that, as stated in [23], this CRB is an average CRB, not a true lower bound, and it is only applicable when M and N are sufficiently large.

TABLE 3: Default variable values

Variable	Value
Carrier frequency f_c	40 GHz
Subcarrier spacing Δf	120 kHz
Number of observations collected N_{CL}	4
Number of sensing frames simulated	2000
Minimum number of bit errors	800
Maximum number of bits simulated	4×10^7
Minimum number of communication frames simulated	200
Number of communication paths L_{com}	3
Number of sensing targets L_{sen}	1
Rician K factor	0 dB
Number of subcarriers M	256
Number of symbol sent per frame N	64
Integer delay and Doppler indices	
Target velocity	$6 \times 7.03 = 42.18$ m/s
Target range	$29 \times 4.88 = 141.52$ m
Fractional delay and Doppler indices	
Target velocity	40 m/s
Target range	140 m
Interpolation factor N_{ML}	4

B. Complexity Analysis

The observation collection algorithm searches through an $N \times M$ matrix for N_{CL} observations. The complexity of such an operation is negligible compared to the other operations of the system, such as the IDFT and DFT utilised by OFDM based transmit pre-processing and receive post-processing.

The interpolation algorithm operates using an $N \times NN_{ML}$ DFT matrix and an $MN_{ML} \times M$ IDFT matrix during the delay and Doppler shift estimation, compared to an $N \times N$ DFT matrix and an $M \times M$ IDFT matrix in the absence of interpolation, leading to an increase in complexity. The complexity of the DFT and IDFT operations depends on the specific implementation utilised, therefore no complexity order is given.

The single-tap demodulation relies on the Maximum Likelihood (ML) detector for IM-OFDM [34], hence it has the same complexity order of $\mathcal{O}(M_G)$. The MMSE demodulation is similar to single-tap demodulation, but with the addition of N matrix inversions applied to matrices of size $M \times M$. The complexity order for matrix inversions is proportional to M^3 [35], but again, it is dependent on the specific implementation utilised.

V. Simulation Results and Discussion

Unless otherwise stated, the simulation parameters used are given in Table 3. The IM-OFDM system is compared to an OFDM benchmark using QPSK modulation. Since classic OFDM activates all the subcarriers, no block interleaving is employed.

Three combinations of M_G and M_A are considered: $M_G = 4$ and $M_A = 3$ (4,3); $M_G = 2$ and $M_A = 1$ (2,1); and $M_G = 4$ and $M_A = 1$ (4,1). To maintain an equal throughput of 2 bits per channel use (bpcu) for the above schemes, (4,3) uses QPSK modulation, (2,1) 8-PSK, and (4,1) 64-QAM.

When the communication signal is received, it is sampled to obtain the discrete received signal. This creates delay bins into which the received signal paths fall into. As a fractional delay index is considered to be equivalent to an integer delay index as long as it lies within the same delay bin, only integer delay indices are considered. This allows the simpler form of the received signal given in (7) to be used, which reduces the simulation duration. This simplification is included because the performance of IM-OFDM communication is well understood, so the focus of this work is on the sensing behaviour.

This assumption is valid for communication as the individual path or paths the signal has travelled through do not have to be separately identified. By contrast, this is not the case for sensing, as each individual propagation path has to be separately identified, because it could be associated with a separate target, as mentioned in Section 1.

For integer indices, the target range and velocity are set to a multiple of the approximate range and velocity resolutions of the system. An approximation is used, as the range and velocity resolutions are a function of c_0, which is not an integer.

The communication Signal to Noise Ratio (SNR) is used for sensing. This is calculated based on the path loss for a communication target at the range shown in the table, in order to illustrate the performance trade-offs between communication and sensing.

The proposed sensing algorithm retains the oldest information. An alternative would be to retain the newest information. To investigate the effect of this choice, consideration is given to the maximum detectable velocity, approximately 225 m/s, and the range resolution in the absence of interpolation, approximately 4.88 m. For the system parameters chosen, the distance traveled over 16 consecutive observations is 0.03 m. This is expected to be insignificant relative to the more coarse resolution of the system. Thus, it can be concluded that the choice of retaining the first or the last information will not materially impact the accuracy of the range estimate. If the interpolation factor is above 64, then the resolution of the system increases to a level where this choice may be revisited.

A. Integer Indices

1) Varying the Number of Observations Collected

The number N_{CL} of observations collected is varied, as shown in Figures 2 and 3. There is an improvement in the RMSE *vs.* SNR trend as N_{CL} is increased, which is in line with expectations as the missing information in the matrix of collected observations is filled in, hence increasing the accuracy of the sensing algorithm. This improvement then

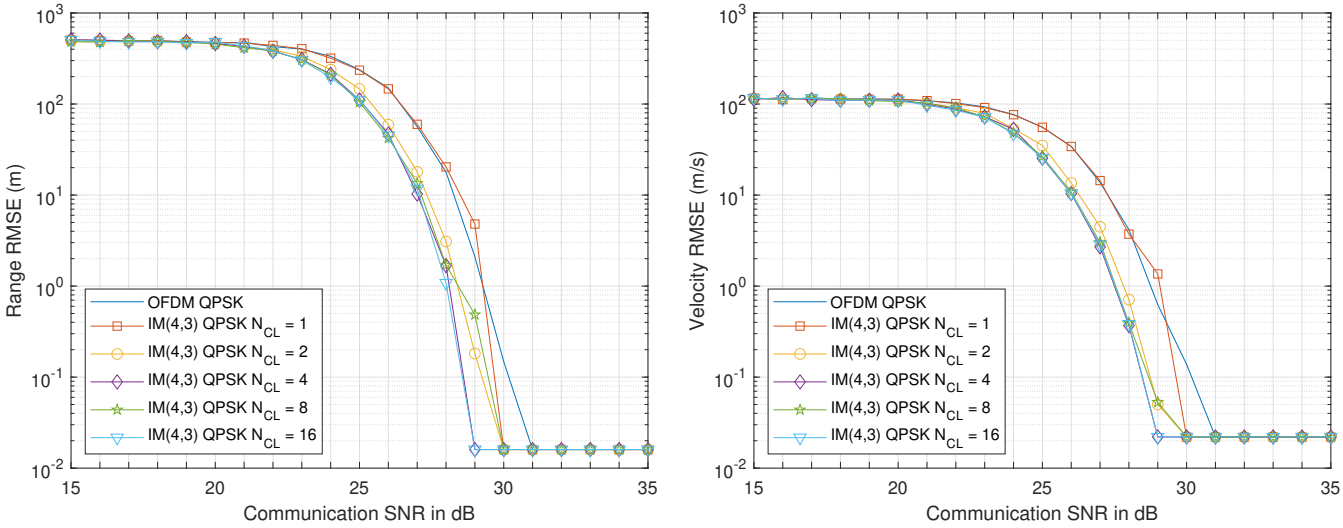

(a) Range RMSE **(b) Velocity RMSE**

FIGURE 2: IM-OFDM(4,3) QPSK RMSE for $N_{CL} = 1, 2, 4, 8, 16$ for integer indices

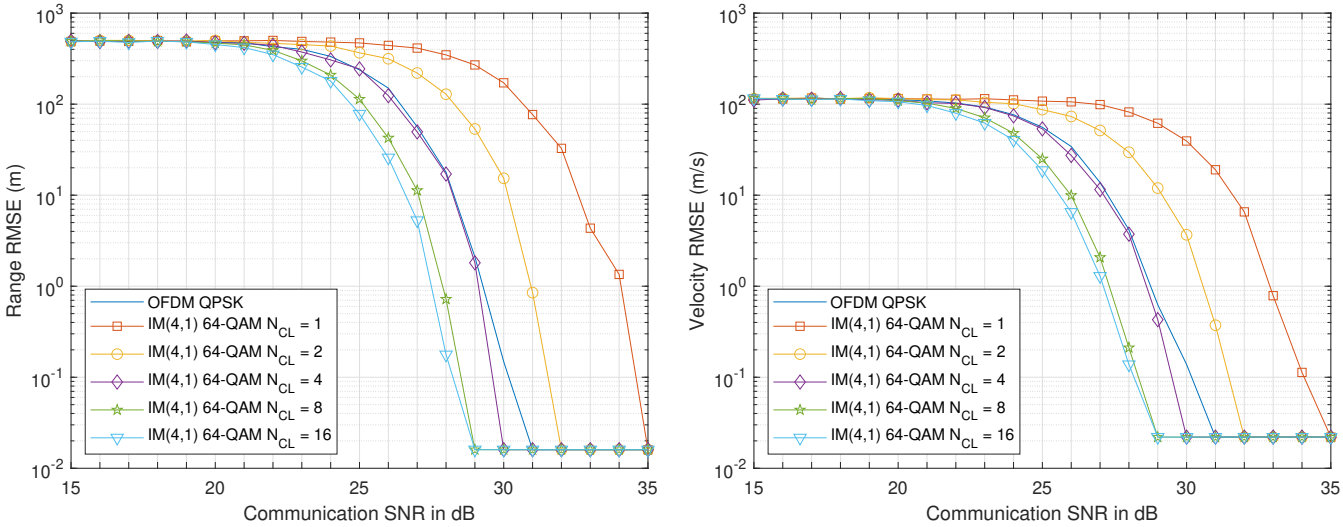

(a) Range RMSE **(b) Velocity RMSE**

FIGURE 3: IM-OFDM(4,1) 64-QAM RMSE for $N_{CL} = 1, 2, 4, 8, 16$ for integer indices

stagnates above certain N_{CL} values. The value of N_{CL} at which this stagnation occurs increases as the number of activated subcarriers is reduced, which is due to the reduction of the information conveyed by using IM.

For both (4,3) and (2,1), increasing N_{CL} beyond 4 has no significant impact on the sensing performance. This is illustrated by the lines lying close to each other throughout the communication SNR range considered, once N_{CL} exceeds this threshold. For (4,1), N_{CL} has to be increased to 8 for the sensing performance to plateau. For all other results in this section, the value of N_{CL} will be set to 4.

As shown in Figures 2 and 3, increasing N_{CL} has no impact on the error floor. This occurs because, firstly, as OFDM sensing assumes relatively low target velocities, where the Doppler shift associated with the target is less than $\frac{\Delta f}{10}$, the target is unlikely to have moved a significant distance whilst the observations are collected, as previously discussed.

Secondly, the size of the sensing imaging matrix is independent of N_{CL}. The sensing resolution is proportional to the size of the imaging matrix. The error floor is the difference between the value output by the estimator and the target parameter value when the noise level is no longer significant.

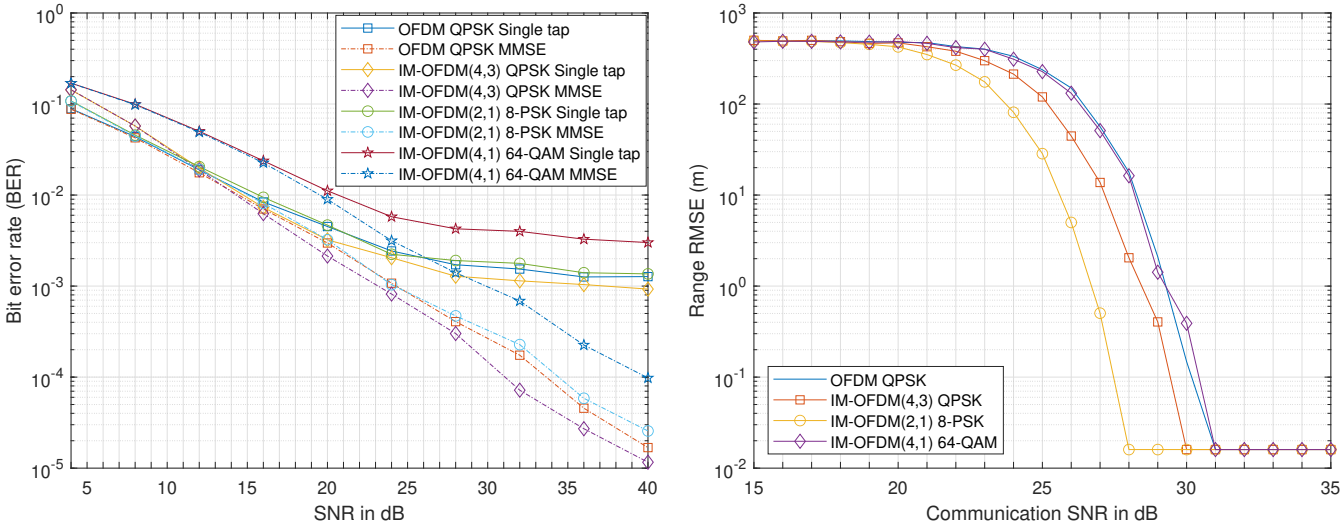

(a) BER for single-tap and MMSE demodulation

(b) Range RMSE for $N_{CL} = 4$

FIGURE 4: BER and range RMSE for OFDM and IM-OFDM for integer indices

As the output of the sensing algorithm is an integer multiple of the system resolution, the error floor is not affected by N_{CL}.

2) Default Values

Figure 4a shows the BER performance of the system for all the configurations considered. The configuration of (4,3) has the lowest BER at higher SNR, followed by OFDM. This is expected, as both the (4,3) and the OFDM schemes have the same modulation order, with the signal power on each activated subcarrier for (4,3) being $\sqrt{\frac{4}{3}}$ instead of 1, where the latter is the case for OFDM. As the number of activated subcarriers is reduced, the modulation order is increased to maintain the total data throughput of 2 bpcu, which erodes the overall BER performance.

Single-tap demodulation exhibits an error floor higher than 8×10^{-4} for all systems, which is unsuited for practical use. MMSE demodulation does not have an error floor and exhibits a lower BER than single-tap demodulation at higher SNRs. The emergence of an error floor for single-tap demodulation is because this algorithm only utilises the diagonal values of the FD channel matrix. By contrast, MMSE demodulation operates on the channel matrix prior to demodulation, as described in Section B. Hence, single-tap demodulation results in an inaccurate demodulation, when a significant Doppler shift is present, which manifests itself as an error floor. This error floor may be mitigated by utilising error correction coding techniques.

Figure 4b characterises the sensing performance of the systems for $N_{CL} = 4$. As the sensing performance is similar for both range and velocity estimation, only the range RMSE is shown. The scheme (2,1) reaches the RMSE error floor at the lowest SNR, followed by the (4,3), OFDM and (4,1) arrangements. As the number of subcarriers activated in an IM block is decreased, the per-carrier power is increased, which in turn increases the detection reliability. At $N_{CL} = 4$, the probability of having missing information in the imaging matrix is low for (2,1) and (4,3), but higher for the (4,1) scheme. Hence, the performance of (4,1) is similar to that of OFDM for $N_{CL} = 4$.

3) Effects of Block Interleaving

The subcarrier block interleaving employed for IM-OFDM separates the grouped subcarriers. This leads to the subcarriers within a group being spread across the available bandwidth, shown in (1), as opposed to having the subcarriers within a group next to each other, as in conventional IM-OFDM. This reduces the probability of all the subcarriers within a group experiencing a deep fade, which increases the activated subcarrier index detection reliability.

Figure 5 shows the BER performance of the IM-OFDM systems both with (w/) and without (w/o) block interleaving, using the OFDM performance as a benchmark. The presence of block interleaving does not make single-tap detection viable for all systems. The performance of the (4,3) and (2,1) schemes is degraded, when no block interleaving is used in support of MMSE demodulation. However, the absence of interleaving does not affect the (4,1) scheme. The performance of (4,3) is worse than that of OFDM, when no block interleaving is employed.

When multiple subcarriers are activated within a group, a more dramatic potential variability is introduced, as the detection algorithms demodulate multiple signals at a time in an attempt to identify the activated subcarriers. The

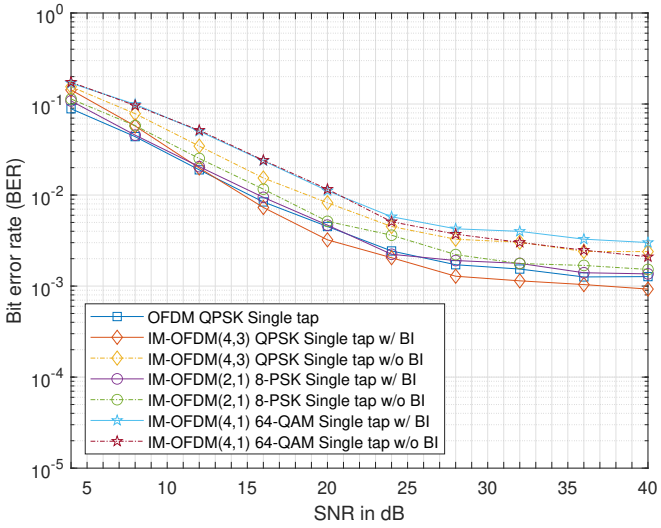

(a) Single-tap demodulation

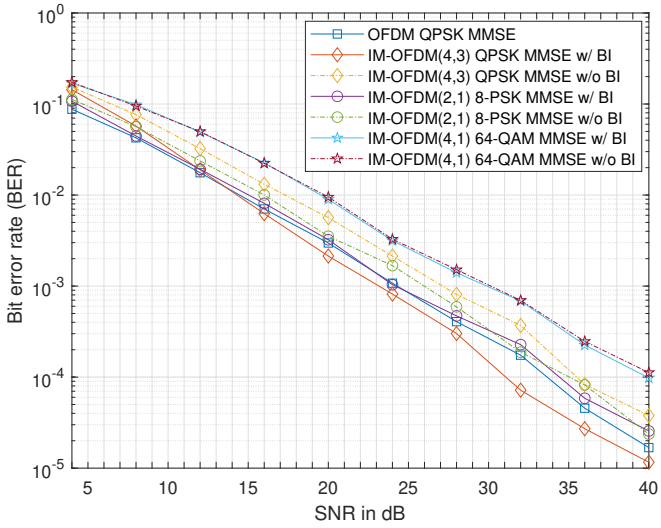

(b) MMSE demodulation

FIGURE 5: BER for single-tap and MMSE demodulation for OFDM and IM-OFDM with (w/) and without (w/o) block interleaving for integer indices

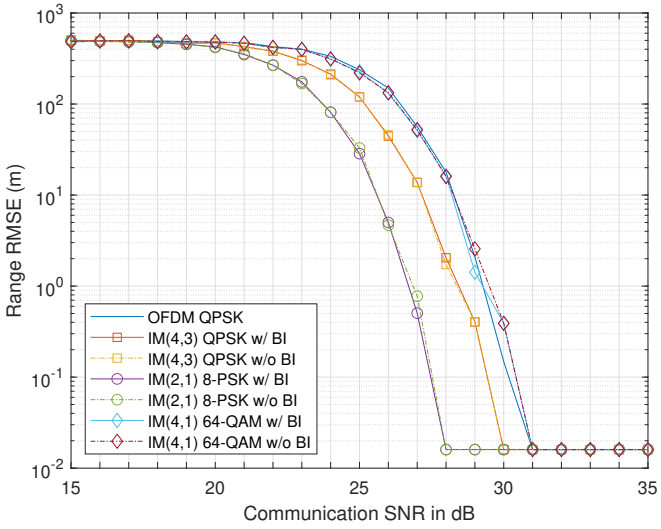

(a) Range RMSE

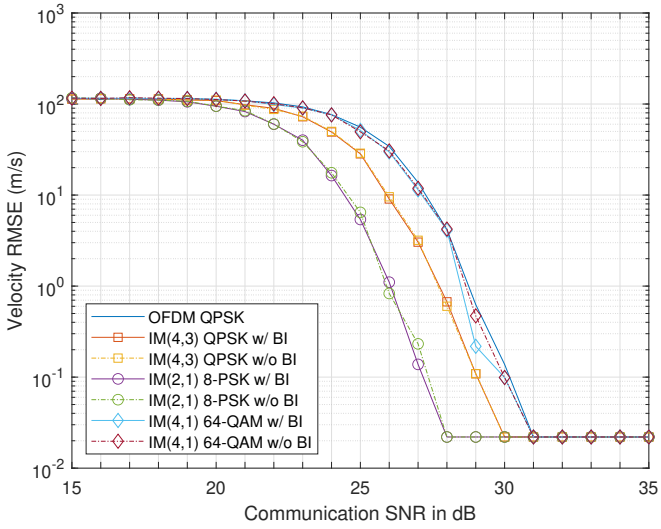

(b) Velocity RMSE

FIGURE 6: RMSE for OFDM and IM-OFDM for $N_{CL} = 4$ with (w/) and without (w/o) block interleaving for integer indices

above-mentioned advantages of block interleaving therefore improve the BER performance attained.

Figure 6 shows that block interleaving has little to no effect on the sensing performance. As the sensing algorithm has *a priori* knowledge of the transmitted signal, and removes the transmitted information from the received signal, the specific ordering of the transmitted data has no effect on the sensing performance.

4) Effects of PSK and QAM Modulation on the Sensing Performance

The effect of the PSK and QAM and their bit per symbol throughput on the sensing performance is shown in Figure 7. Increasing the modulation order has little effect on the sensing performance of PSK, but degrades the sensing performance as the QAM order is increased. It can also be seen that QAM reaches the RMSE error floor at a higher SNR than PSK modulation.

Again, these trends occur due to the QAM symbols' variable amplitude. When the data is removed from the

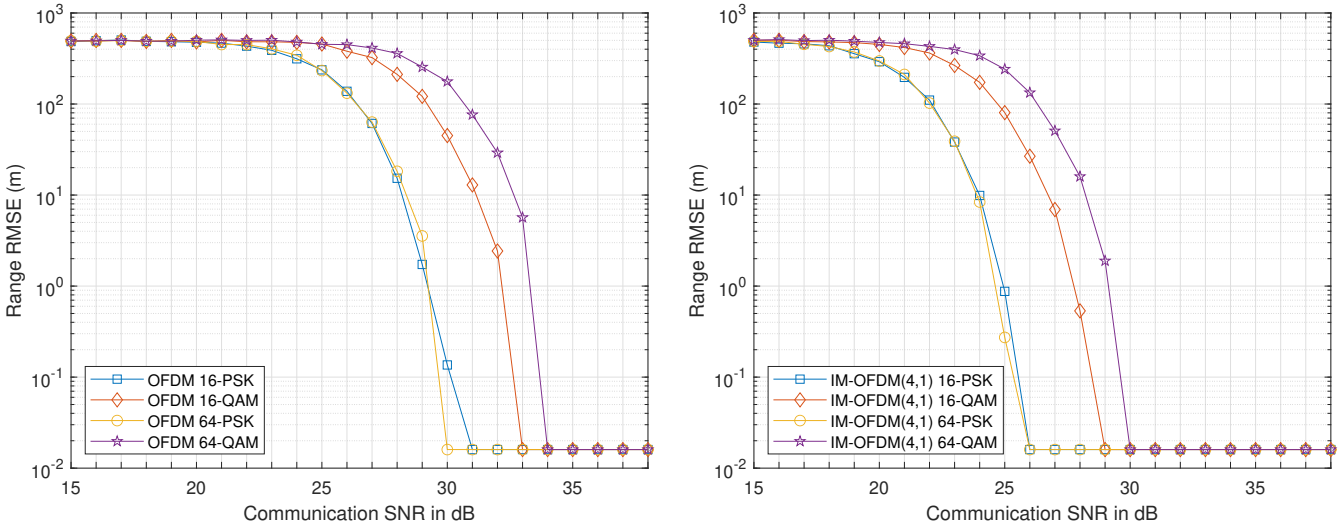

(a) OFDM **(b) IM-OFDM(4,1)**

FIGURE 7: Range RMSE for modulation of 16- and 64-PSK and 16- and 64-QAM for integer indices

received sensing signal, the time-frequency matrix produced will have noise levels that are less statistically uniform, due to the varied amplitude of the data symbols. Once this matrix is converted to the DD, these varied noise levels reduce the detection reliability by increasing the probability of false peaks.

These results are supported by [36], which investigates the effect of the transmit signal randomness on the sensing performance attained. As QAM varies both the amplitude and phase of a signal, it produces a signal for sensing that is more "random" than PSK, which only varies the phase, but not the magnitude.

5) Effects of Increasing the Number of Objects on the Sensing Performance

To characterise the system's sensing performance in more complex environments, simulations have been performed where 3 additional reflecting objects have been added that are not desired targets. The range and velocity of these additional objects are randomly chosen to be: R_2 = 175.68 m, R_3 = 175.68 m, R_4 = 219.6 m, V_2 = -14.06 m/s, V_3 = 70.3 m/s, and V_4 = -21.09 m/s. The sensing RMSE results recorded for a single target and for multiple objects are shown in Figure 8.

Although the sensing performance of all the systems is reduced when additional reflective objects are introduced, their relative sensing performance remains similar. The performance reduction is due to the additional peaks in the DD image matrix corresponding to the additional objects, hence requiring a smaller noise amplitude for an erroneous target estimation.

6) Comparison with Partial-Activation Based OFDM

The use of IM in the spatial domain is shown to result in a lower system performance than other techniques [37]. To demonstrate the effectiveness of IM in the FD, partial-activation based OFDM is investigated. By activating only a subset of the available subcarriers for OFDM, the modulation order on the activated subcarriers has to be increased to maintain the system throughput for a fair comparison. IM provides an additional dimension to transmit information, thereby allowing the modulation order to remain the same as for standard OFDM. Therefore, IM-OFDM will always have the potential to outperform OFDM partial subcarrier activation for communication and sensing.

To illustrate this, an additional partial-activation based OFDM benchmark scheme has been created: OFDM-3/4. This schemes employs OFDM, whilst only activating three-quarters of the subcarriers, without employing index modulation. Since fewer subcarriers are used, the power on the activated subcarriers is increased by a factor of $\frac{4}{3}$. To maintain the throughput of 2 bpcu, OFDM-3/4 uses QPSK, QPSK, and 16-QAM on each group of three activated subcarriers, and it is compared to IM-OFDM(4,3) QPSK.

The BER results of MMSE demodulation are shown in Figure 9a. The increased modulation order of OFDM-3/4 leads to a higher BER than that of IM-OFDM(4,3) and OFDM for SNRs above 10 dB. The BER of partial-activation based OFDM is higher than that of IM-OFDM for the majority of the SNR range considered.

Since partial-activation based OFDM does not transmit on all subcarriers, there is some missing target information, similarly to IM-OFDM. Since partial-activation based OFDM always transmits on the same subcarriers, the collection algorithm would not "fill in" the missing information. Thus,

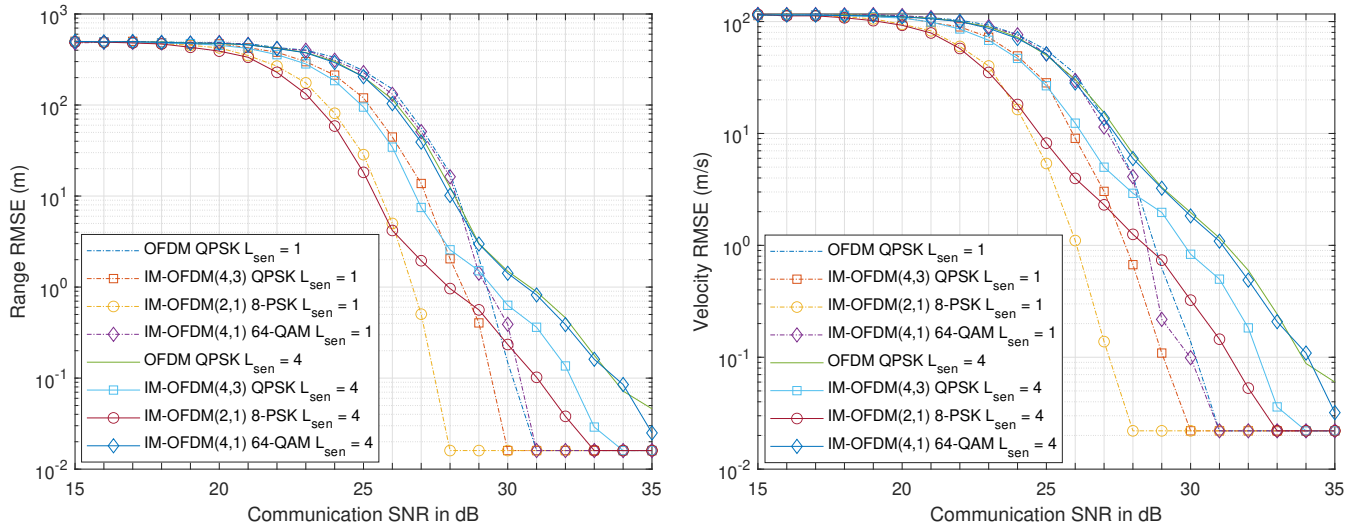

(a) Range **(b) Velocity**

FIGURE 8: Sensing RMSE of the OFDM and IM-OFDM systems for one target L_{sen} = 1 and multiple objects L_{sen} = 4

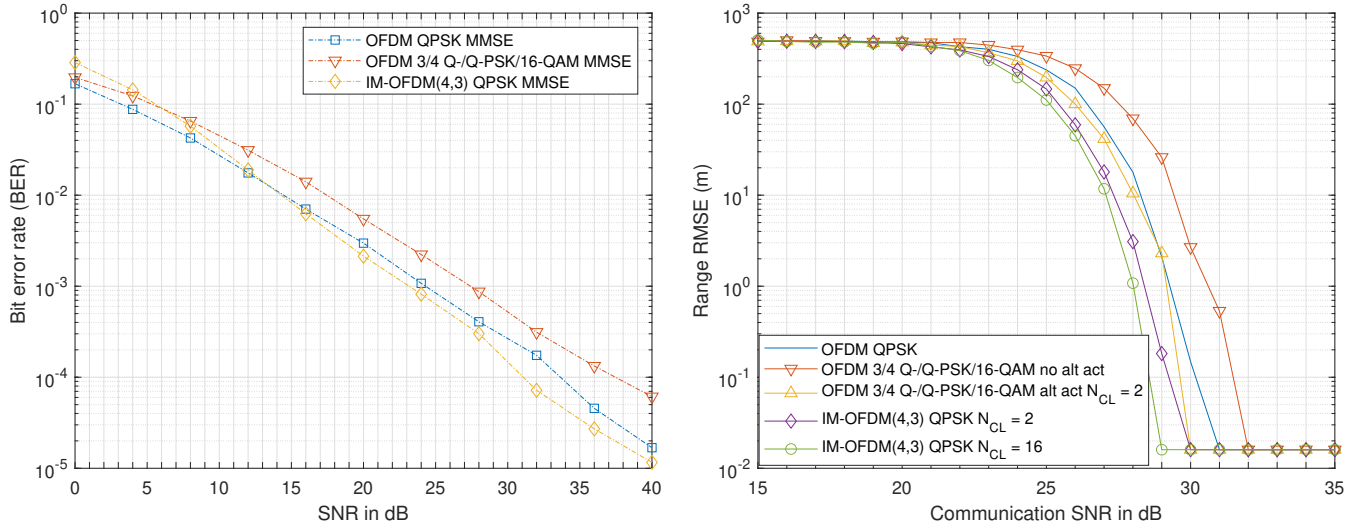

(a) BER **(b) Range RMSE**

FIGURE 9: BER and range RMSE of OFDM QPSK, OFDM-3/4 QPSK QPSK 16-QAM and IM-OFDM(4,3) QPSK

partial-activation based OFDM would never outperform its equivalent IM-OFDM system for sensing.

The sensing performance of partial-activation based OFDM can be improved if there is an alternating subcarrier activation pattern, which increases the system complexity. This modification arranges for partial-activation based OFDM to alternate between multiple sets of subcarriers. For OFDM-3/4, two sets of subcarriers are considered. This allows the system to receive full target information, once two observations are collected. The range RMSE of sensing is shown in Figures 9b. For partial-activation based OFDM, "no alt act" refers to the system operating without alternating activation. By contrast, "alt act" represents the system employing alternating activation.

OFDM-3/4 operating without alternating activation reaches the RMSE error floor at a higher SNR than OFDM, since the amplitude variation of the individual QAM symbols reduces the sensing performance, despite the increased power on the activated subcarriers. When alternating activation is used, OFDM-3/4 reaches the error floor at the same SNR as IM-OFDM(4,3) using $N_{CL} = 2$, since the amplitude variation of 16-QAM offsets the performance improvement from receiving full target

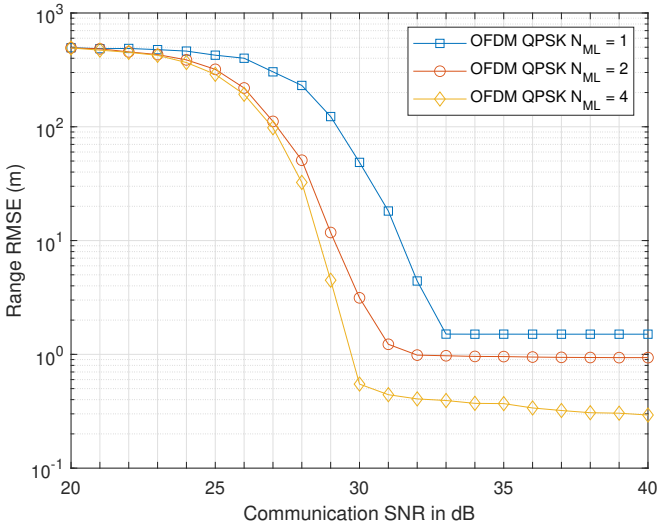

(a) Range RMSE

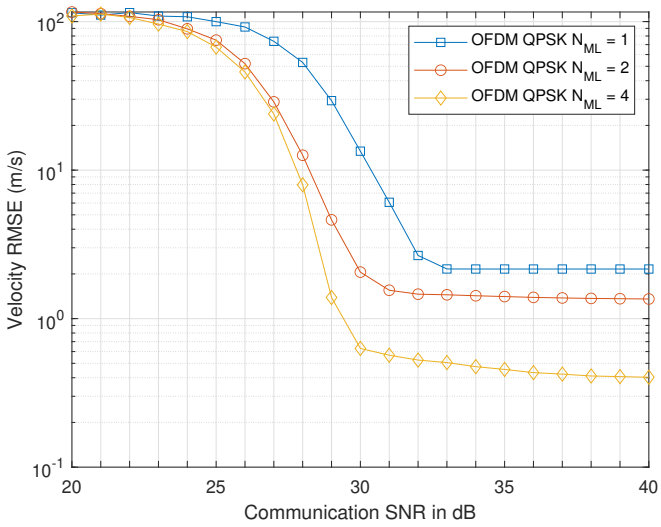

(b) Velocity RMSE

FIGURE 10: OFDM QPSK RMSE for $N_{ML} = 1, 2, 4$ for fractional indices

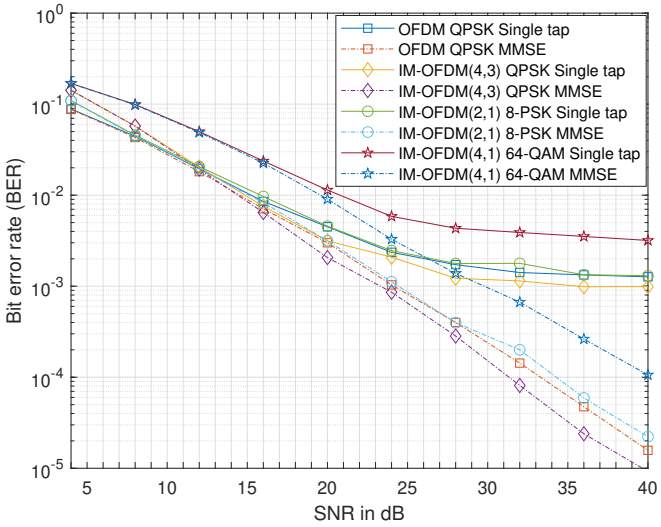

(a) BER for single-tap and MMSE demodulation

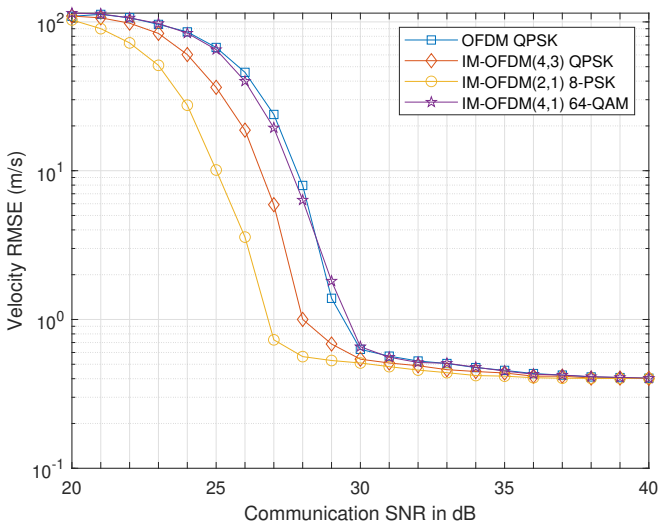

(b) Velocity RMSE for $N_{CL} = 4$ for $N_{ML} = 4$

FIGURE 11: BER and velocity RMSE for OFDM and IM-OFDM for fractional indices

information. IM-OFDM(4,3) using $N_{CL} = 16$ outperforms OFDM-3/4 employing alternating activation.

Thus, IM-OFDM is capable of outperforming partial-activation based OFDM for both sensing and communication, even when a more complex alternating activation pattern is employed.

B. Fractional Indices

1) Varying the Interpolation Factor

The effect of varying N_{ML} on the RMSE is shown in Figure 10 for OFDM. The trends are similar for all the other considered systems, hence only the OFDM results are shown. The error floor is higher than for integer indices, because there is a larger discrepancy between the estimator output values and the target parameters. As N_{ML} is increased, both the error floor and the SNR at which the error floor is reached are reduced. This is because the system resolution is increased as N_{ML} is increased.

2) Default Values

Figure 11a shows the BER performance of the system for all the configurations considered for integer delay and fractional Doppler indices. The trends in Figure 11a are identical to

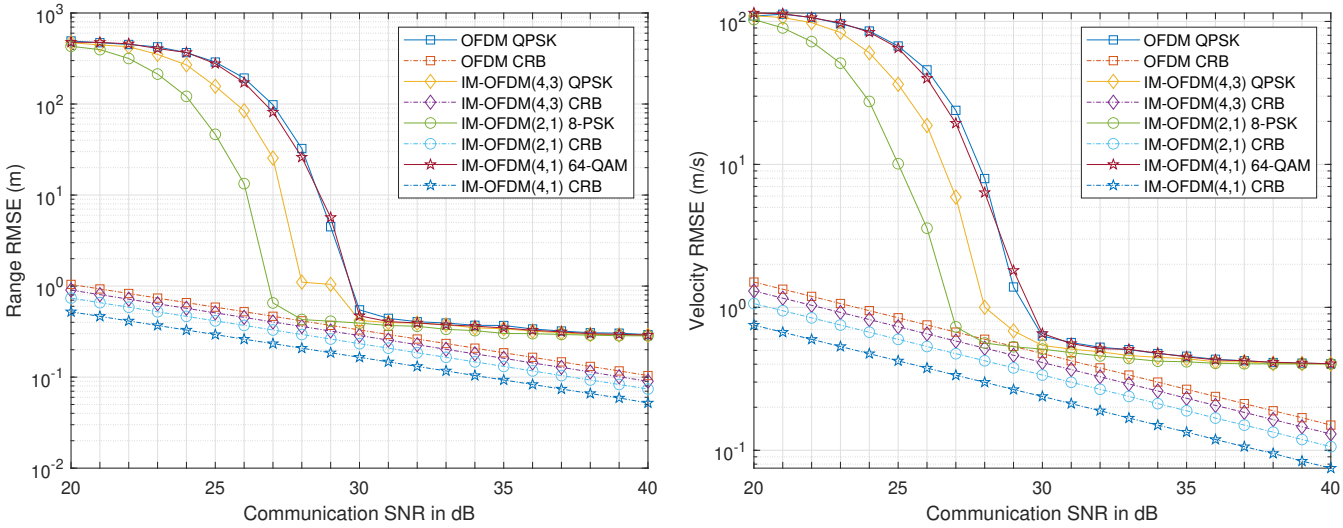

(a) Range RMSE **(b) Velocity RMSE**

FIGURE 12: CRB and RMSE for OFDM and IM-OFDM for $N_{CL} = 4$ for $N_{ML} = 4$ for fractional indices

TABLE 4: Results Summary for Default Integer Index Values

System	SNR at which the RMSE error floor is reached	SNR at which 10^{-4} BER is reached
OFDM QPSK	31 dB	33.5 dB
IM-OFDM(4,3) QPSK	30 dB	31 dB
IM-OFDM(2,1) 8-PSK	28 dB	34.5 dB
IM-OFDM(4,1) 64-QAM	31 dB	40 dB

the those of integer indices, shown in Figure 4a. Switching from integer to fractional Doppler indices has no effect on the BER of the systems.

Figure 11b shows the range RMSE performance of all systems for $N_{ML} = 4$. The trends across the systems are the same as observed for integer indices in Figure 4b, with the (2,1) scheme having the best performance, followed by the (4,3) scheme, with the OFDM benchmark and the (4,1) scheme.

C. Cramér-Rao Bound

The CRB with the RMSE results of the systems considered are shown in Figure 12, for the default fractional index values. As the CRB assumes having a complete set of information concerning the reflected signal, the system having the highest average power on each activated subcarrier, namely (4,1), has the lowest CRB. By contrast, the OFDM benchmark has the highest CRB. The systems (2,1), (4,3) and OFDM approach their respective CRBs as they reach their error floors, but they then diverge from the CRB as the SNR increases. Further, the RMSE of the (4,1) scheme does not approach its CRB, because too few observations are collected to fully exploit the increased power of each activated subcarrier of this IM configuration.

D. Peak-to-Average Power Ratio

The Peak-to-Average Power Ratio (PAPR) of the TD transmitted signals of the OFDM and IM-OFDM systems have been calculated over 20,000 frames, with the Complementary Cumulative Distribution Function (CCDF) of the PAPR for $M = 4$, 16, 64, and 256 subcarriers shown in Figure 13. Although the power assigned to the activated subcarriers is increased in the FD for IM-OFDM, this does not necessarily lead to an increase in the PAPR in the TD, since the blank/deactivated subcarriers reduce the likelihood of a peak generated by the IDFT used in the conversion from FD to TD. The PAPR of IM-OFDM is lower than that of OFDM for a small number of subcarriers, but approaches the PAPR of OFDM as the number of subcarriers is increased. Thus, the use of IM does not increase the PAPR of OFDM, but reduces it when a small number of subcarriers is employed, and remains unchanged when a large number of subcarriers is utilised.

VI. Conclusions and Future Work

A novel IM-OFDM ISAC solution was conceived, which outperforms OFDM ISAC by collecting multiple sensing observations. The delay caused by the collection of multiple observations has no impact on the sensing performance, as the error floors remain constant when N_{CL} is varied. For

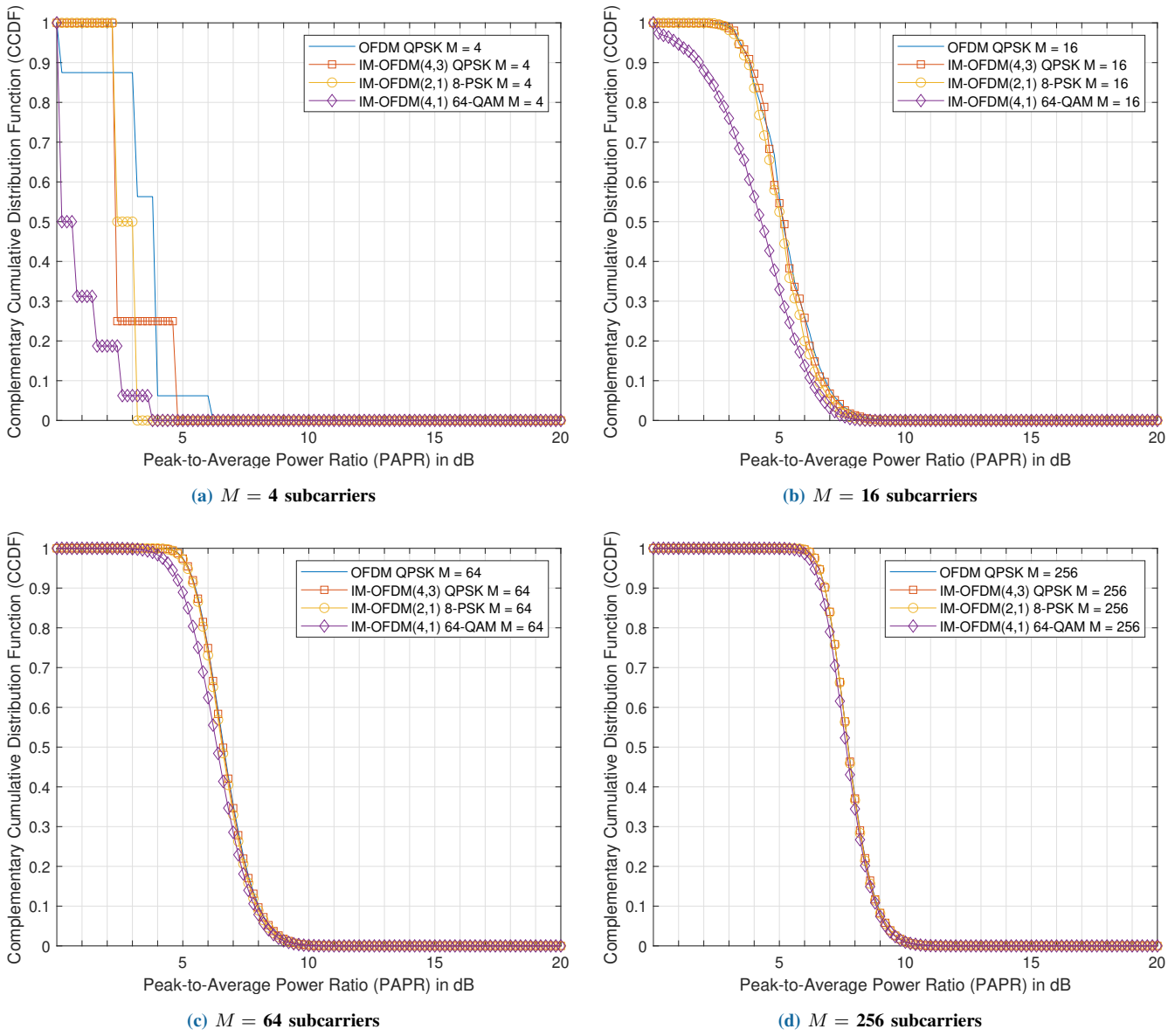

(a) $M = 4$ **subcarriers**

(b) $M = 16$ **subcarriers**

(c) $M = 64$ **subcarriers**

(d) $M = 256$ **subcarriers**

FIGURE 13: CCDF of the PAPR of all the considered systems

$N_{CL} = 4$, the (4,3) scheme is shown to outperform OFDM both in terms of sensing and communication. A summary of the results for the default integer index scenario is shown in Table 4.

A range of trade-offs was characterised in terms of the subcarrier grouping, communication throughput, and the number of sensing observation collected. If a modest sensing and communication performance improvement is deemed sufficient, the (4,3) configuration may be recommended. If a higher sensing performance is desired at the cost of communication performance erosion, the (2,1) or (4,1) schemes may be employed, depending on the target velocity and the required throughput. It can also be seen that the (4,1) scheme using PSK modulation has a better sensing performance than the other systems. As noted in the complexity analysis, the demodulation complexity is proportional to the number of subcarriers in a group, with (2,1) having the lowest demodulation complexity amongst the IM-OFDM systems.

Increasing the interpolation factor leads to a similar improvement in sensing performance in all systems, albeit at the cost of increased complexity. Increasing M and N will also increase the sensing resolution, but would require a substantial system modification.

Future work will include the definition of a combination of IM and OTFS, as well as analysing the performance trade-offs associated with this combination for ISAC. As noted in Section 2, the communication performance of the systems may be improved by error correction codes. Deci-

sion directed detection will be investigated, utilising iterative exchange of information between the communication and sensing algorithms. This would allow the communication and sensing algorithms to share information with each other, in order to improve their respective performances.

REFERENCES

[1] A. Salsbury, "Safeguarding Vessels by Radio," *Popular Science Monthly*, vol. 88, pp. 451–453, 1916. [Online]. Available: https://books.google.fr/books?id=giYDAAAAMBAJ&printsec=frontcover&hl=fr&source=gbs_ge_summary_r&cad=0#v=onepage&q&f=false

[2] A. O. Bauer, "Some Historical and Technical Aspects of Radio Navigation in Germany, Over the Period 1907 to 1945," 2004. [Online]. Available: https://www.cdvandt.org/Navigati.pdf

[3] H. G. Schantz, "On the Origins of RF-Based Location," in *2011 IEEE Topical Conference on Wireless Sensors and Sensor Networks*, 2011, pp. 21–24.

[4] D. S. Ilčev, "New Aspects of Progress in the Modernization of the Maritime Radio Direction Finders (RDF)," *Transactions on Maritime Science*, vol. 10, no. 1, p. 68–83, Apr. 2021. [Online]. Available: https://www.toms.com.hr/index.php/toms/article/view/359

[5] R. M. Mealey, "A Method for Calculating Error Probabilities in a Radar Communication System," *IEEE Transactions on Space Electronics and Telemetry*, vol. 9, no. 2, pp. 37–42, 1963.

[6] Y. Liu, G. Liao, J. Xu, Z. Yang, and Y. Zhang, "Adaptive OFDM Integrated Radar and Communications Waveform Design Based on Information Theory," *IEEE Communications Letters*, vol. 21, no. 10, pp. 2174–2177, 2017.

[7] D. Ma, N. Shlezinger, T. Huang, Y. Liu, and Y. C. Eldar, "Joint Radar-Communication Strategies for Autonomous Vehicles: Combining Two Key Automotive Technologies," *IEEE Signal Processing Magazine*, vol. 37, no. 4, pp. 85–97, 2020.

[8] A. Hassanien, M. G. Amin, Y. D. Zhang, and F. Ahmad, "Signaling strategies for dual-function radar communications: an overview," *IEEE Aerospace and Electronic Systems Magazine*, vol. 31, no. 10, pp. 36–45, 2016.

[9] Y. Cui, F. Liu, X. Jing, and J. Mu, "Integrating Sensing and Communications for Ubiquitous IoT: Applications, Trends, and Challenges," *IEEE Network*, vol. 35, no. 5, pp. 158–167, 2021.

[10] L. Zheng and D. Tse, "Diversity and multiplexing: a fundamental tradeoff in multiple-antenna channels," *IEEE Transactions on Information Theory*, vol. 49, no. 5, pp. 1073–1096, 2003.

[11] J. Li and P. Stoica, "MIMO Radar with Colocated Antennas," *IEEE Signal Processing Magazine*, vol. 24, no. 5, pp. 106–114, 2007.

[12] L. Godara, "Application of Antenna Arrays to Mobile Communications Part II. Beam-Forming and Direction-of-Arrival Considerations," *Proceedings of the IEEE*, vol. 85, no. 8, pp. 1195–1245, 1997.

[13] M. M. Şahin, I. E. Gurol, E. Arslan, E. Basar, and H. Arslan, "OFDM-IM for Joint Communication and Radar-Sensing: A Promising Waveform for Dual Functionality," *Frontiers in Communications and Networks*, vol. 2, p. 34, 2021. [Online]. Available: https://www.frontiersin.org/article/10.3389/frcmn.2021.715944

[14] P. Kumari, J. Choi, N. González-Prelcic, and R. W. Heath, "IEEE 802.11ad-Based Radar: An Approach to Joint Vehicular Communication-Radar System," *IEEE Transactions on Vehicular Technology*, vol. 67, no. 4, pp. 3012–3027, 2018.

[15] C. Sturm and W. Wiesbeck, "Waveform Design and Signal Processing Aspects for Fusion of Wireless Communications and Radar Sensing," *Proceedings of the IEEE*, vol. 99, no. 7, pp. 1236–1259, 2011.

[16] X. Chen, Z. Feng, Z. Wei, P. Zhang, and X. Yuan, "Code-Division OFDM Joint Communication and Sensing System for 6G Machine-Type Communication," *IEEE Internet of Things Journal*, vol. 8, no. 15, pp. 12 093–12 105, 2021.

[17] Z. Ni, J. Andrew Zhang, K. Yang, X. Huang, and T. A. Tsiftsis, "Multi-Metric Waveform Optimization for Multiple-Input Single-Output Joint Communication and Radar Sensing," *IEEE Transactions on Communications*, pp. 1–1, 2021.

[18] Y. Zeng, Y. Ma, and S. Sun, "Joint Radar-Communication: Low Complexity Algorithm and Self-Interference Cancellation," in *2018 IEEE Global Communications Conference (GLOBECOM)*, 2018, pp. 1–7.

[19] M. Temiz, E. Alsusa, and M. W. Baidas, "A Dual-Functional Massive MIMO OFDM Communication and Radar Transmitter Architecture," *IEEE Transactions on Vehicular Technology*, vol. 69, no. 12, pp. 14 974–14 988, 2020.

[20] ——, "Optimized Precoders for Massive MIMO OFDM Dual Radar-Communication Systems," *IEEE Transactions on Communications*, vol. 69, no. 7, pp. 4781–4794, 2021.

[21] ——, "A Dual-Function Massive MIMO Uplink OFDM Communication and Radar Architecture," *IEEE Transactions on Cognitive Communications and Networking*, vol. 8, no. 2, pp. 750–762, 2022.

[22] J. B. Sanson, D. Castanheira, A. Gameiro, and P. P. Monteiro, "Cooperative Method for Distributed Target Tracking for OFDM Radar With Fusion of Radar and Communication Information," *IEEE Sensors Journal*, vol. 21, no. 14, pp. 15 584–15 597, 2021.

[23] L. Gaudio, M. Kobayashi, G. Caire, and G. Colavolpe, "On the Effectiveness of OTFS for Joint Radar Parameter Estimation and Communication," *IEEE Transactions on Wireless Communications*, vol. 19, no. 9, pp. 5951–5965, 2020.

[24] K. Wu, J. A. Zhang, X. Huang, and Y. J. Guo, "OTFS-Based Joint Communication and Sensing for Future Industrial IoT," *IEEE Internet of Things Journal*, pp. 1–1, 2021.

[25] H. Zhang, T. Zhang, and Y. Shen, "Modulation Symbol Cancellation for OTFS-Based Joint Radar and Communication," in *2021 IEEE International Conference on Communications Workshops (ICC Workshops)*, 2021, pp. 1–6.

[26] A. Şahin, S. S. M. Hoque, and C.-Y. Chen, "Index Modulation With Circularly-Shifted Chirps for Dual-Function Radar and Communications," *IEEE Transactions on Wireless Communications*, vol. 21, no. 5, pp. 2938–2952, 2022.

[27] T. Huang, N. Shlezinger, X. Xu, Y. Liu, and Y. C. Eldar, "MAJoRCom: A Dual-Function Radar Communication System Using Index Modulation," *IEEE Transactions on Signal Processing*, vol. 68, pp. 3423–3438, 2020.

[28] T. Huang, N. Shlezinger, X. Xu, D. Ma, Y. Liu, and Y. C. Eldar, "MultiCarrier Agile Phased Array Radar," *IEEE Transactions on Signal Processing*, vol. 68, pp. 5706–5721, 2020.

[29] M. Li and W.-Q. Wang, "Joint Radar-Communication System Design Based on FDA-MIMO via Frequency Index Modulation," *IEEE Access*, vol. 11, pp. 67 722–67 736, 2023.

[30] W. Baxter, E. Aboutanios, and A. Hassanien, "oint Radar and Communications for Frequency-Hopped MIMO Systems," *IEEE Transactions on Signal Processing*, vol. 70, pp. 729–742, 2022.

[31] G. Huang, Y. Ding, S. Ouyang, and V. Fusco, "Index modulation for OFDM RadCom systems," *The Journal of Engineering*, vol. 2021, no. 2, pp. 61–72, 2021. [Online]. Available: https://ietresearch.onlinelibrary.wiley.com/doi/abs/10.1049/tje2.12003

[32] C. Xu, L. Xiang, J. An, C. Dong, S. Sugiura, R. G. Maunder, L.-L. Yang, and L. Hanzo, "OTFS-Aided RIS-Assisted SAGIN Systems Outperform Their OFDM Counterparts in Doubly Selective High-Doppler Scenarios," *IEEE Internet of Things Journal*, vol. 10, no. 1, pp. 682–703, 2023.

[33] L. Gaudio, M. Kobayashi, B. Bissinger, and G. Caire, "Performance Analysis of Joint Radar and Communication using OFDM and OTFS," in *2019 IEEE International Conference on Communications Workshops (ICC Workshops)*, 2019, pp. 1–6.

[34] C. Xu, Y. Xiong, N. Ishikawa, R. Rajashekar, S. Sugiura, Z. Wang, S.-X. Ng, L.-L. Yang, and L. Hanzo, "Space-, Time- and Frequency-Domain Index Modulation for Next-Generation Wireless: A Unified Single-/Multi-Carrier and Single-/Multi-RF MIMO Framework," *IEEE Transactions on Wireless Communications*, vol. 20, no. 6, pp. 3847–3864, 2021.

[35] G. Golub and C. Loan, *Matrix Computations*, 3rd ed. Baltimore and London: The Johns Hopkins University Press, 1996.

[36] Y. Xiong, F. Liu, Y. Cui, W. Yuan, T. X. Han, and G. Caire, "On the Fundamental Tradeoff of Integrated Sensing and Communications Under Gaussian Channels," *IEEE Transactions on Information Theory*, vol. 69, no. 9, pp. 5723–5751, 2023.

[37] B. Gaede, A. Bereyhi, S. Asaad, and R. R. Mueller, "A Fair Comparison Between Spatial Modulation and Antenna Selection in Massive MIMO Systems," in *WSA 2019; 23rd International ITG Workshop on Smart Antennas*, 2019, pp. 1–6.

Hugo Hawkins (Graduate Student Member, IEEE) received his B.Eng. degree in Electrical and Electronic Engineering from the University of Southampton with First Class Honours in 2021. He is currently undertaking a PhD within the Next Generation Wireless Research Group at the University of Southampton. His research interests include integrated sensing and communication.

Chao Xu (S'09-M'14-SM'19) received the B.Eng. degree in telecommunications from the Beijing University of Posts and Telecommunications, Beijing, China, the B.Sc. (Eng.) degree (with First Class Hons.) in telecommunications from the Queen Mary, University of London, London, U.K., through a Sino-U.K. joint degree Program in 2008, and the M.Sc. degree (with distinction) in radio frequency communication systems and the Ph.D. degree in wireless communications from the University of Southampton, Southampton, U.K., in 2009 and 2015, respectively. He is currently a Senior Lecturer with Next Generation Wireless Research Group, University of Southampton. His research interests include index modulation, reconfigurable intelligent surfaces, noncoherent detection, and turbo detection. He was recipient of the Best M.Sc. Student in Broadband and Mobile Communication Networks by the IEEE Communications Society (United Kingdom and Republic of Ireland Chapter) in 2009. He was also the recipient of 2012 Chinese Government Award for Outstanding Self-Financed Student Abroad and 2017 Dean's Award, Faculty of Physical Sciences and Engineering, the University of Southampton. In 2023, he was awarded Marie Sklodowska-Curie Actions (MSCA) Global Postdoctoral Fellowships with the highest evaluation score of 100/100.

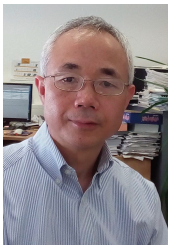

Lie-Liang Yang (Fellow, IEEE) is the professor of Wireless Communications in the School of Electronics and Computer Science at the University of Southampton, UK. He received his MEng and PhD degrees in communications and electronics from Northern (Beijing) Jiaotong University, Beijing, China in 1991 and 1997, respectively, and his BEng degree in communications engineering from Shanghai TieDao University, Shanghai, China in 1988. He has research interest in wireless communications, wireless networks and signal processing for wireless communications, as well as molecular communications and nano-networks. He has published 400+ research papers in journals and conference proceedings, authored/co-authored three books and also published several book chapters. The details about his research publications can be found at https://www.ecs.soton.ac.uk/people/llyang. He is a fellow of the IEEE, IET and AAIA, and was a distinguished lecturer of the IEEE VTS. He served as an associate editor to various journals, and is currently a senior editor to the IEEE Access and a subject editor to the Electronics Letters. He also acted different roles for organization of conferences.

LAJOS HANZO (Life Fellow, IEEE) Lajos Hanzo (FIEEE'04) received Honorary Doctorates from the Technical University of Budapest (2009) and Edinburgh University (2015). He is a Foreign Member of the Hungarian Science-Academy, Fellow of the Royal Academy of Engineering (FREng), of the IET, of EURASIP and holds the IEEE Eric Sumner Technical Field Award. For further details please see http://www-mobile.ecs.soton.ac.uk, https://en.wikipedia.org/wiki/Lajos_Hanzo